Contents lists available at ScienceDirect

Geochimica et Cosmochimica Acta

Archean to early Paleoproterozoic iron formations document a transition in iron oxidation mechanisms

Changle Wang [a,b,c,*], Leslie J. Robbins [b,d], Noah J. Planavsky [b], Nicolas J. Beukes [f], Laureline A. Patry [g], Stefan V. Lalonde [g], Maxwell A. Lechte [h], Dan Asael [b], Christopher T. Reinhard [i], Lianchang Zhang [a,c], Kurt O. Konhauser [e]

[a] *Key Laboratory of Mineral Resources, Institute of Geology and Geophysics, Chinese Academy of Sciences, Beijing, China*
[b] *Department of Earth and Planetary Sciences, Yale University, New Haven, USA*
[c] *College of Earth and Planetary Sciences, University of Chinese Academy of Sciences, Beijing, China*
[d] *Department of Geology, University of Regina, Regina, SK, Canada*
[e] *Department of Earth and Atmospheric Sciences, University of Alberta, Edmonton, Canada*
[f] *DST-NRF CIMERA, Department of Geology, University of Johannesburg, South Africa*
[g] *European Institute for Marine Studies, CNRS-UMR6538 Laboratoire Géosciences Océan, Technopôle Brest-Iroise, Plouzané, France*
[h] *Department of Earth and Planetary Sciences, McGill University, Montréal, Canada*
[i] *School of Earth and Atmospheric Sciences, Georgia Institute of Technology, Atlanta, USA*

ARTICLE INFO

ABSTRACT

It is generally accepted that photosynthetic marine planktonic bacteria were responsible for the oxidation of dissolved ferrous iron (Fe(II)) and the subsequent deposition of iron formations (IFs) throughout the Archean and early Paleoproterozoic. However, the relative roles of the different biological Fe oxidation mechanisms in driving IF deposition—such as anoxygenic photosynthesis (photoferrotrophs) and oxygenic photosynthesis (cyanobacteria)—remain poorly resolved. Here, we present coupled bulk-rock Fe isotope and manganese (Mn) versus Fe ratios from Archean to early Paleoproterozoic IFs in order to provide a new perspective on Earth's early redox history and processes leading to IF deposition. Based on this updated IF geochemical record, we bolster the case that the partial oxidation of Fe(II) to Fe(III) was central to IF genesis, arguing against extensive water column Fe(II) silicate formation as the main process driving IF deposition. The geochemistry of IFs deposited prior to the Great Oxidation Event (GOE) shows that partial Fe(II) oxidation was a common feature in either anoxic or low oxygen (O_2) conditions, where metabolic Fe(II) oxidation by photoferrotrophs is likely to have prevailed over ambient Fe(II) oxidation by O_2 produced by cyanobacteria. Assuming that cyanobacteria evolved in the Archean, the presence of partial Fe(II) oxidation suggests that O_2 production was relatively muted during this time. This points to a model for Archean surface redox conditions, whereby oxygen oases were relatively limited in extent, likely due to low primary productivity of cyanobacteria and high Fe fluxes. We further demonstrate a gradual displacement of metabolic Fe(II) oxidation in the Archean by quantitative O_2-driven Fe(II) oxidation during the GOE by ca. 2.31 Ga.

© 2022 Elsevier Ltd. All rights reserved.

1. Introduction

The atmosphere during the first half of Earth's 4.5-billion-year (Ga) history was essentially devoid of free oxygen (O_2), with atmospheric abundances<0.0001 % of the present atmospheric level (PAL) (Farquhar et al., 2011; Lyons et al., 2014; Catling and Zahnle, 2020). Geological and geochemical constraints reveal that the first permanent rise in the partial pressure of atmospheric O_2 (pO_2) occurred between $\sim$ 2.5 and 2.3 Ga, a period that has been termed the Great Oxidation Event (GOE) (e.g., Bekker et al., 2004; Holland, 2006; Warke et al., 2020). Despite widespread agreement on these general trends, the tempo and mode of Earth's early oxygenation, and the redox conditions leading up to the GOE, remain poorly understood as few redox proxies are sufficiently precise to track secular variations in ocean–atmosphere O_2 abundance. At a minimum, the oxygenation of the atmosphere may have coincided with the emergence of oxygenic photosynthesis (Fischer et al., 2016; Rasmussen et al., 2019; Slotznick et al., 2022), but it is more

* Corresponding author at: Key Laboratory of Mineral Resources, Institute of Geology and Geophysics, Chinese Academy of Sciences, Beijing, China.
E-mail address: wangcl@mail.iggcas.ac.cn (C. Wang).

commonly assumed that incipient oxygenation of Earth's surface environments occurred hundreds of millions of years before the GOE (e.g., Anbar et al., 2007; Koehler et al., 2018). The latter view is supported, among other arguments, by some recent molecular phylogenomic studies (Sánchez-Baracaldo and Cardona, 2020), which point to an Archean origin for the rise of stem cyanobacteria, as well as antioxidant enzymes (Boden et al., 2021) and enzymes that either produce or utilize O_2 which points to an Archean origin for oxygenic photosynthesis (Jabłońska and Tawfik, 2021). These biological timelines are consistent with several geochemical proxies, indicating an Archean origin for oxygenic photosynthesis (e.g., Lyons et al. 2014). However, part of the difficulty in reconstructing ocean–atmosphere redox evolution is that the different sensitivities of these various proxies mean that they may not respond uniformly to changes in pO_2 (Anbar et al., 2007; Koehler et al., 2018). This debate on the onset and timing of Earth's early oxidation has also given rise to recent questions as to what role biological oxidation played, if any, in the deposition of iron formations (IFs).

Iron formations are particularly useful sedimentary archives for tracking Fe sources and sinks, as well as marine redox conditions, because during much of the Archean and early Paleoproterozoic they formed in a range of depositional settings on the continental shelves of existing cratons (Bekker et al., 2010, 2014; Konhauser et al., 2017). Moreover, because IF are chemical sediments, they represent an archive of seawater chemistry at the time of their deposition (Konhauser et al., 2017), which can in turn, provide insights into the availability of trace-element nutrients to, and the activity of, the ancient biosphere (Robbins et al., 2016). The best-preserved IF successions have a remarkably uniform mineralogy, composed mostly of chert, magnetite, and hematite, with variable amounts of Fe-rich silicate minerals (e.g., greenalite, stilpnomelane, riebeckite), carbonate minerals (e.g., siderite, ankerite), and locally, sparse sulfides (e.g., pyrite). The observed mineral assemblages in IFs likely reflect the culmination of multiple processes including marine authigenesis, diagenesis, and post-depositional alteration processes. The primary precipitates are generally believed to have been a mixture predominantly composed of amorphous silica (Si) and ferric (Fe(III)) oxyhydroxides (e.g., ferrihydrite) linking IF genesis to marine ferrous Fe (Fe(II)) oxidation (Konhauser et al., 2017). Greenalite and siderite likely made up a significant fraction of some iron formations, and these minerals are commonly linked to diagenetic processes (Bekker et al., 2014; Konhauser et al., 2017). Alternatively, Fe(II) silicate minerals (namely greenalite), have been suggested to be the principal primary precipitate of IFs (e.g., Tosca et al., 2016; Muhling and Rasmussen, 2020), arguing that the Fe(III) oxide phases of IFs instead represent the product of post-depositional oxidation. Additionally, mixed Fe(II)/Fe(III) minerals, namely green-rusts, have also been proposed as a precursor to magnetite in IFs (Halevy et al., 2017; Li et al., 2017).

For models invoking Fe(II) oxidation, the presence of Fe(III) minerals in IFs is generally ascribed to the activity of planktonic bacteria in the photic zone of Earth's ancient oceans. The classic model invokes Fe(III) precipitation occurring at the interface between oxygenated shallow waters and upwelling Fe(II)-rich waters, with O_2 being sourced from cyanobacteria, or their predecessors (Cloud, 1973). These cyanobacteria would have flourished when sufficient nutrients were available and passively induced the precipitation of Fe(III)-oxyhydroxide through the excretion of their metabolic waste (i.e., O_2). Under high O_2 conditions Fe(II) reacts directly with free O_2 in seawater, and under low O_2 (microaerobic) conditions this process is slow and can be mediated by chemolithoautotrophic Fe(II) oxidizing bacteria (e.g., Field et al., 2016). Alternatively, anoxygenic photoautotrophic Fe(II)-oxidizing bacteria (known as photoferrotrophs) could have directly oxidized Fe(II), coupled to the fixation of carbon utilizing energy

from sunlight (Garrels et al., 1973). From a mass balance perspective, any of these metabolisms could account for all of the Fe(III) deposited in IF given reasonable estimates for microbial cell densities (Konhauser et al., 2002, 2018). As an alternative to biological models for Fe(II) oxidation, Cairns-Smith (1978) proposed that under anoxic conditions the large inventory of Fe(III) in IFs could be produced by Fe(II) ultraviolet (UV) photochemical oxidation. While this mechanism continues to be highlighted in the literature (e.g., Tabata et al., 2021), experiments focused on determining the rates of Fe(II) photochemical oxidation did not simulate the complex, disequilibrium water chemistry characteristic of an Archean ocean where Fe(II)- and Si-rich hydrothermal waters mixed with ambient Si-saturated and high-HCO_3^- seawater (Konhauser et al., 2007). Importantly, under conditions that better approximate Archean seawater composition, the rate of UV photochemical oxidation was found to be negligible relative to the precipitation of Fe(II) silicates and Fe(II) carbonates (Konhauser et al., 2007), suggesting that from a mass balance perspective this mechanism could not sufficiently account for the Fe(III) in IFs. Therefore, although it remains possible that UV photochemical oxidation contributed to IF precipitation, this mechanism seems unlikely to have generated a significant fraction of the Fe(III) deposited in large IFs. Additionally, the view that Fe(II) oxidation drove IF genesis is challenged by suggestions that IFs were largely deposited as Fe(II) silicates (e.g., Muhling and Rasmussen, 2020). Contention regarding the origin and paleoredox significance of IFs has given rise to debate over the possible role of biological oxidation and, by extension, the timing of Earth's early oxygenation and the evolution of carbon fixation throughout Earth history.

1.1. Iron and manganese oxidation

As Fe in seawater is soluble under anoxic conditions as Fe(II) and poorly soluble under oxic conditions (precipitating readily as Fe(III)-oxyhydroxides), the secular record of Fe(II) oxidation may potentially be leveraged to track surface O_2 levels (e.g., Li et al., 2013). However, given that Fe(II) oxidation by photoferrotrophs can proceed under anoxic conditions, this relationship is not necessarily straightforward, particularly for IFs deposited prior to the GOE. One potential means by which we can parse the mechanisms underpinning Fe(II) oxidation in the ancient oceans is through measurement of the relative abundances of the different stable isotopes of Fe in the Fe-oxides (e.g., hematite and magnetite) of IFs (Czaja et al., 2013). This approach is appealing since the kinetics of Fe(II) oxidation are well-constrained and the Fe isotope systematics of Fe(II) oxidation by photoferrotrophs and ambient O_2 are relatively well-understood (Busigny et al., 2014; Croal et al., 2004; Johnson et al., 2020). Briefly, partial oxidation of dissolved Fe(II) produces Fe(III)-oxyhydroxides that are enriched in ^{56}Fe, typically by 1 to 3 ‰, leaving the residual dissolved Fe(II) ^{56}Fe-depleted, although more rapid oxidation effectively lowers this overall fractionation (e.g., Beard et al., 2010; Wu et al., 2011; 2012; Swanner et al., 2017). This degree of fractionation is considered to be the sum of an equilibrium fractionation effect between aqueous Fe(II) and aqueous Fe(III), and a kinetic fractionation associated with the precipitation rate of solid Fe(III) oxyhydroxides from aqueous Fe(III) (see Balci et al., 2006; Johnson et al., 2020). The kinetic fractionation is smaller for the most rapid Fe(II)-oxidation experiments and becomes progressively larger for slower oxidation experiments, resulting in the $\Delta^{56}Fe_{Fe(II)-Fe(III) \text{ oxide}}$ being the largest (least negative) at the most rapid oxidation rates and progressively smaller (most negative) at the slower oxidation rates (Johnson et al., 2020). By contrast, the formation of reduced Fe phases (e.g., Fe carbonates and green-rust) is typically considered to involve either a negligible fractionation or a small negative fractionation (Wiesli et al., 2004), leaving residual dissolved Fe(II)

slightly ^{56}Fe-enriched. When Fe(II) oxidation is complete and quantitative—such as in water columns where there is a sharp redoxcline and a well-oxygenated surface layer—there is no net fractionation during the formation of Fe(III)-oxyhydroxides (Busigny et al., 2014). Therefore, positively fractionated Fe isotope signatures can potentially be used to fingerprint partial Fe(II) oxidation (e.g., Dauphas et al. 2017).

As the fractionation factors of Fe isotopes for Fe(II) oxidation by O$_2$ and anoxygenic photosynthesis effectively overlap (Croal et al., 2004; Wu et al., 2011, 2012), it is difficult to clearly recognize the mechanism responsible for Fe(II) oxidation at different points in Earth's history based on solely Fe isotopes. Further, because kinetic isotope effects associated with the authigenesis of Fe(II) minerals (such as pyrite) and microbially induced Fe(III) reduction can also lead to large negative fractionations (Archer and Vance, 2006; Guilbaud et al., 2011; Rolison et al., 2018; Marin-Carbonne et al., 2020), further evidence is needed to unravel the isotopic record of Fe(II) oxidation from the rock record (Heard and Dauphas, 2020). In sum, another proxy is needed.

Similar to Fe, Mn is redox-sensitive and soluble under anoxic conditions. The oxidation of Mn(II) and the subsequent formation of Mn(III/IV) oxides (from herein simply referred to as Mn oxides) in the presence of O$_2$ generally requires both higher redox potentials than the oxidation of Fe(II) and the catalyzing activity of a Mn(II)-oxidizing bacteria (Tebo et al., 2005; Lyons et al., 2020). Manganese oxides, precipitated in oxygenated surface waters, would also be expected to undergo rapid reductive dissolution in anoxic, Fe(II)-rich seawater, coupled to the oxidation of Fe(II) or organic matter (e.g., Hongve, 1997). This means that, in essence, Fe(II) is also available to react with O$_2$. Alternatively, there are also anaerobic pathways of Mn(II) oxidation: (1) anoxygenic photosynthesis with Mn(II) as electron donors yielding oxidized forms of this metal as a by-product (Daye et al., 2019) and (2) sunlight-catalyzed photochemical oxidation of either rhodochrosite by UV radiation (Liu et al., 2020) or Mn(II) by Fe oxides (Jung et al., 2021). However, Daye et al. (2019) only demonstrate this activity in active microbial cultures that grow in the presence of nanomolar concentrations and modern microorganisms are not known to anaerobically oxidize Mn(II). Further, the culture requires the presence of relatively high levels of sulfide, a condition largely incompatible with IF precipitation. For the latter photochemical oxidation, Liu et al. (2020) only investigated this mechanism in pure water, so whether it could potentially be operable in more complex solution remains to be seen—this was also one of the key challenges to UV photochemical oxidation of Fe(II) (e.g., Konhauser et al., 2007) as a viable mechanism.

There is not much evidence supporting the widespread presence of either Mn carbonate or Mn oxide minerals in Archean oceans (Lyons et al., 2020). In fact, the reports are sparse other than those limited to the time around GOE immediately following the Archean. Authigenic sedimentary Mn enrichments are typically preserved as Mn(II) carbonates such as rhodochrosite, and this is typically linked to primary Mn oxide reduction in the sediment pile during diagenesis (Maynard, 2010), although it has been suggested that sedimentary Mn(II) carbonates may have formed in a redox stratified water column (Siahi et al., 2020; Wittkop et al., 2020). In any case, Mn enrichments result from a Mn oxide shuttle from the water column and require the presence of O$_2$ in at least the surface waters. Given that the oxidation of upwelling Mn(II) is slow compared to the preferentially oxidized Fe(II) (Busigny et al., 2014), abundant Mn oxide precipitation in surface waters (evidenced by secular trends in the relative enrichment of Mn in IFs; i.e., Mn/Fe ratios) may potentially be tied to the evolution of the marine redox state. However, it is not easy to discern the Mn oxide burial only based on the magnitude of either Mn/Fe ratios or Mn contents of sediments, because in Archean oceans the anoxic

condition is able to concentrate soluble Mn(II) to relatively high levels (estimated at 3 to 7 µM; Holland, 1984) so that primary well-preserved Archean carbonates have elevated Mn levels relative to typical Phanerozoic carbonates (e.g., Veizer, 1978; Fischer and Knoll, 2009).

Because IFs serve as robust archives of both the Fe isotope compositions and Mn/Fe ratios in the deep time (Kurzweil et al., 2016), these parameters may be interrogated to constrain the redox state of local seawater during IF deposition. Importantly, a correlation between these two parameters argues for the presence of free O$_2$ in seawater (Kurzweil et al., 2016) and suggests that Fe isotope fractionation is associated with water column oxidation, with concomitant Fe–Mn oxide formation, as supported by observations and geochemical data from modern redox-stratified lakes (Busigny et al., 2014). In ancient water columns characterized by widespread partial Fe(II) oxidation (e.g., Li et al., 2013; Wang et al., 2022), the upwelling and the partial oxidation of ferruginous deep water would cause the continuous depletion of heavy Fe isotopes in the remaining Fe(II) reservoir until the reservoir is exhausted in most proximal settings (Tsikos et al., 2010; Kurzweil et al., 2016). Therefore, the Fe oxides that precipitate from the more proximal Fe(II) pool should show relatively low Fe isotope compositions. Additionally, in these setting there should be comparatively elevated O$_2$ levels (if present) and this could have oxidized Mn(II) and precipitated Mn oxides, potentially transferring the Mn enrichment to the local sediments with a depleted Fe isotopic signature (e.g., Wang et al., 2022).

Coupled Fe and Mn records are therefore likely to be critical for tracking the timing and the evolution of O$_2$-driven Fe(II) and Mn(II) oxidation across Earth's history. In order to investigate the possible role of biologically driven redox reactions during IF precipitation, and the corresponding insights into oxygenation in the lead-up to the GOE, we explore the IF record of Fe isotope and Mn to Fe ratio proxies spanning the Archean and early Paleoproterozoic. Temporal variations in the Fe isotopes and Mn/Fe ratios reported here point towards a gradual shift from the anoxygenic oxidation of Fe by photoferrotrophs in the Archean to quantitative O$_2$-driven oxidation in the Paleoproterozoic during the GOE.

2. Geological background

Archean—Paleoproterozoic IF and ironstone samples were collected from surface outcrop and drill cores in seven localities: the ∼ 3.7 Ga Isua greenstone belt (West Greenland), ∼3.2 Ga Barberton greenstone belt (South Africa), ∼2.94 Ga Red Lake greenstone belt (Canada), ∼2.56 Ga Eastern Hebei (North China), ∼2.55 Ga Qingyuan greenstone belt (North China), ∼2.5–2.4 Ga Hamersley Basin (Western Australia), and ∼ 2.5–2.3 Ga Transvaal Basin (South Africa). Information about the geological setting, petrography, and sedimentology of these IFs and ironstones is documented below.

2.1. The 3700 Ma Isua greenstone belt (West Greenland)

The Isua greenstone belt is located in the southern West Greenland and contains the world's largest accumulation of Eoarchean metavolcanics and metasedimentary rocks (Polat and Frei, 2005). These supracrustal rocks have all undergone polyphase metamorphism from the early Archean through to the early Proterozoic, and currently display uppermost greenschist to lower amphibolite facies metamorphic assemblages (Nutman et al., 1984; Rollinson, 2003). The northern part of the belt was divided into three different lithotectonic domains: Northwestern, Central, and Southeastern (Appel et al., 1998; Myers, 2001). The domain of least strain, the central tectonic domain, contains small areas of

well-preserved volcanic and sedimentary features, including pillow basalts, pillow breccia, heterogeneous volcanic breccia, banded iron formation (BIF), and polymictic conglomerate (Nutman et al., 2002). Most BIF layers are thin, with separation of quartz and magnetite ± amphibole into distinct anastomosing mesobands (Nutman et al., 2017). This tectonic fabric was produced by the destruction and transposition of original sedimentary layering during strong ductile deformation under amphibolite facies metamorphism.

The depositional age of the BIF is constrained by U–Pb geochronological studies of a few detrital zircon grains from cherts associated with BIF (3694 ± 4 Ma) (Nutman et al., 2002) and of a few zircons extracted from interlayered volcanic ash (3707 ± 6 Ma) (Nutman et al., 1997).

2.2. The 3200 Ma Moodies Group, Barberton greenstone belt (South Africa)

The Barberton greenstone belt (BGB) is situated in the central-east part of South Africa, along the border between the Mpumalanga Province and Swaziland (Fig. S2). The succession of rocks that comprise the BGB was subdivided into three different groups (Fig. S2-S3). The bottom Onverwacht Group (3.55–3.28 Ga) is predominantly composed of mafic and ultramafic volcanic rocks and some thin cherty units thought to be sedimentary in origin (Bontognali et al., 2013; Lowe and Byerly, 1999). The Fig Tree Group (3.28–3.23 Ga) occurs between the volcanic Onverwacht Group and the overlying siliciclastic Moodies Group and is composed of greywacke, shale, chert, minor jasper/carbonate/barite, and felsic volcanic rocks. The Fig Tree Group was deposited in a variety of alluvial, fan delta, and deep- and shallow-water environments (Lowe, 2013). Previous work on the ferruginous chert (jasper) suggested that there was no evidence that the Fe was secondary, and therefore was interpreted to be a primary chemical sediment (Hofmann, 2005). Although Satkoski et al. (2015) found different Fe isotope compositions between high-Fe chert and low-Fe chert to argue for a redox stratified ocean, other workers obtained contrasting results (Planavsky et al., 2012; Busigny et al., 2017) (Fig. S4). The Moodies Group (3.23–3.2 Ga) consists of alluvial to shallow-marine sandstones, mudstones, minor conglomerates, and discrete intercalations of BIF (Heubeck and Lowe, 1999). Although the metamorphic grade of the BGB is constrained to lower greenschist facies and metamorphic temperatures could have reached ∼ 320 °C (Nabhan et al., 2017), multiple regional alteration events have affected the greenstone belt during the Archean and Paleoproterozoic following burial (Heubeck, 2019).

The BIF is thinly interbedded with fine-grained and cross-stratified sandstones, indicating shallow-water deposition; however, the fine laminations in the BIF suggest that they were still deposited below wave base. Thus, the BIF may have been deposited in a shallow, current-swept environment. The dominant iron-rich minerals within BIF are hematite and magnetite, with less common occurrences of Fe-carbonate phases (mainly ankerite). Petrographic textures reveal that hematite constitutes an early mineral phase, while magnetite and ankerite display textures indicative of a late diagenetic or metamorphic origin (Bontognali et al., 2013).

A synopsis of the available U-Pb zircon dates from air-fall, water-reworked tuffs, and cross-cutting dikes for the Moodies Group suggests that deposition began around 3224 ± 1 Ma and ended by about 3209 ± 14 Ma (Heubeck, 2019).

2.3. The 2940 Ma Red Lake greenstone belt (Canada)

The Red Lake greenstone belt is located in the Superior Province on the southern margin of the Uchi Subprovince within the North Caribou Terrane. The Ball Assemblage of this belt is comprised of a dominantly calc-alkaline mafic to felsic volcanic sequence with minor komatiite, siliciclastics, BIF, and stromatolitic carbonates (McIntyre and Fralick, 2017; Sanborn-Barrie et al., 2001). The carbonate platform comprises BIF, stromatolitic carbonates, and siliciclastic sedimentary rocks such as black shale, siltstone, and conglomerate (Afroz, 2019), which are overlain and underlain by mafic to felsic volcanic rocks. The BIF is closely associated with carbonate rocks and is characterized by magnetite interbedded with chert. The absence of carbonate and slumped rock due to downward intermittent movement of rock debris and the presence of volcanic rocks above BIF suggest that BIF were deposited distal from the carbonate platform, possibly, in the deep water of an upper slope setting (Afroz, 2019). The metamorphic grade is constrained to greenschist-to-amphibolite facies.

The age of the carbonate platform is constrained by U-Pb zircon ages from an underlying rhyolitic lapilli tuff (2940 ± 2 Ma) and an overlying rhyolitic flow (2925 ± 3 Ga) (Corfu and Wallace, 1986).

2.4. The 2565 Ma Xiaolaihe iron formation, Qingyuan greenstone belt (China)

The Qingyuan greenstone belt is located on the northern margin of the North China Craton (NCC) and consists dominantly of late Neoarchean plutons and supracrustal rocks. These supracrustal rocks are subdivided into three formations (from the bottom up): Shipengzi, Hongtoushan, and Nantianmen formations. The Xiaolaihe BIF occurs in the upper part of the Shipengzi Formation and is interbedded with *meta*-volcanic rocks (*meta*-basalts and -dacites), which have undergone granulite facies metamorphism (Peng et al., 2018, 2019). The Xiaolaihe BIF consists of alternating magnetite- and silicate-rich microbands (0.05–5 mm thick), among which individual bands are straight and continuous. The mineral assemblage is composed of magnetite, quartz, pyroxene, cummingtonite, and minor calcite.

The age of this BIF is constrained by SIMS U-Pb zircon dating of a biotite plagioclase gneiss (*meta*-dacite) interlayer (2565 ± 8 Ma; Peng et al., 2019).

2.5. The 2540 Ma Sijiaying iron formation, Luanxian Group (China)

In China, BIFs occur extensively throughout the Archean-Paleoproterozoic units of the NCC. Eastern Hebei, in the north, is considered to be the second largest iron metallogenic province after Anshan-Benxi in the NCC (Wang et al., 2017). A large number of BIFs are exposed in Eastern Hebei, such as the Shuichang, Shirengou, Erma, Xingshan, Sijiaying, and Macheng BIFs. The Sijiaying BIF is the largest and laterally most extensive BIF in Eastern Hebei and occurs in the lower succession of the Luanxian Group. This group comprises upper greenschist- to lower amphibolite-facies metamorphosed volcanic and sedimentary rocks. They are dominated by biotite plagioclase gneiss, biotite leptynite, amphibolites, and minor garnet hornblende leptynite. The intermediate-felsic *meta*-volcanic rocks up to hundreds of meters thick are intercalated with the Sijiaying BIF of various thicknesses from<10 m to hundreds of meters (Wang et al., 2017). The BIF consists of successive quartz-rich (white) and magnetite-rich (black) bands of between < 1 and 50 mm thickness. A few centimeter-scale mesobands are composed of several millimeter-scale microbands. The mineral assemblage is simple, consisting predominantly of quartz and magnetite with lesser amounts of actinolite and hornblende.

Cui et al. (2014) reported three SIMS U-Pb zircon dates for *meta*-volcanic rocks associated with the BIF that constrain the depositional age. These include a *meta*-dacitic flow (hornblende plagioclase gneiss) at the base of the BIF sequence which yielded an age of 2543 ± 14 Ma, a 2537 ± 13 Ma *meta*-dacitic tuffaceous rock

(biotite leptynite) interlayered with the BIF further up, and a 2535 ± 8 Ma *meta*-andesite lava flow (biotite plagioclase gneiss) within the upper part of the sedimentary succession.

2.6. The 2500–2440 Ma iron formations, Hamersley Group (Western Australia)

The Hamersley Group comprises almost 2.5 km of continuous sedimentary and volcanic rocks located within the ∼ 80,000 km² Hamersley Province of the Pilbara Craton in northwestern Australia (Fig. S5). In the lower part, it consists of dolomite, shale, and BIF, while the upper part consists of dolerite, various lava types, and BIF with minor amounts of tuffs and shales (Trendall and Blockley, 1970).

The Brockman Iron Formation of the Hamersley Group is divided into four units, namely the lowermost Dales Gorge Member (BIF), the Whaleback Shale Member, the Joffre Member (BIF), and the uppermost Yandicoogina Shale Member (Fig. S6). After deposition, these laterally extensive BIF have all experienced minor folding and basinal uplift along with low-grade regional metamorphism, from burial prehnite-pumpellyite facies to greenschist facies (Smith et al., 1982). The consensus view is that the Brockman Iron Formation was deposited on a large, stable, and clastic-starved continental platform, which was only influenced by episodic inputs of fine-grained tuffaceous detritus (Gross, 1983; Morris and Horwitz, 1983).

On the basis of SHRIMP U-Pb ages from zircons extracted from tuffaceous bands (Trendall et al., 2004) and a Re-Os age of the underlying black shale of the Mount McRae Shale (Anbar et al., 2007), a depositional age between 2500 and 2460 Ma is proposed for the Dales Gorge Member. This unit is composed of 33 alternating hematite-magnetite-chert and chert-carbonate–silicate macrobands. Within the decimeter- to meter-scale macrobands, there are centimeter-scale mesobands and laminated microbands of Fe oxides, Fe silicates, Fe carbonates, and chert, with minor amounts of pyrite and organic carbon. Iron-rich bands are characterized by massive anhedral aggregates and xenomorphic hematite, commonly showing overgrowths of subhedral magnetite with minor apatite and late diagenetic ankerite-Fe dolomite. Iron-poor bands consist of fine-grained quartz, siderite, and Fe-talc in variable amounts (Pecoits et al., 2009).

Based on the dominant mineralogy, five lithological subdivisions within the Joffre BIF were defined (Haugaard et al., 2016): oxide BIF, silicate-carbonate-oxide BIF, stilpnomelane-rich tuffaceous mudrock, stilpnomelane mudrock, and calcareous mudrock. Besides chert and magnetite, the prominent mineralogy is riebeckite, ankerite, hematite, stilpnomelane, and crocidolite. Pickard (2002) documented two SHRIMP U-Pb zircon ages from interbedded tuffaceous mudrocks at the top and base of the Joffre BIF succession, that are 2454 ± 3 Ma and 2459 ± 3 Ma, respectively.

Similar to the Dales Gorge Member of the Brockman Iron Formation, the overlying Weeli Wolli Formation also contains BIF, in which mesobands of chert alternate with mesobands of magnetite and/or hematite (Trendall, 1973). Trendall et al. (2004) published a SHRIMP U-Pb age of zircons from tuffaceous rocks in this formation (2445 ± 5 Ma), representing the age of the BIF in the Weeli Wolli Formation.

The Boolgeeda Iron Formation in the upper part of the Hamersley Group also hosts BIF layers. Geochronological constraints on the deposition of this formation include a U-Pb zircon age of 2450 ± 3 Ma for the conformably underlying Woongarra Rhyolite (Trendall et al., 2004) and a maximum detrital zircon U-Pb age of 2460 ± 9 Ma for a meter-scale layer of diamictite in the Boolgeeda Iron Formation (Caquineau et al., 2018). The BIF is composed of Fe oxides (mostly magnetite and minor hematite), quartz, and lesser amounts of carbonate, with minor chlorite and rare muscovite.

Banding on the cm-scale is most clearly defined by alternating quartz and Fe-oxide rich layers (Warchola et al., 2018).

2.7. The 2500–2310 Ma iron formations, Transvaal Supergroup (South Africa)

Strata of the Transvaal Supergroup, deposited on the Kaapvaal craton, are preserved in two structural basins (Fig. S7): the Eastern Transvaal (or northeastern) sub-basin and the Griqualand West (or southwestern) sub-basin. The Transvaal Supergroup in the Griqualand West sub-basin consists mainly of a chemical sedimentary rock package (Ghaap Group) unconformably overlain by a mixed volcanic-chemical-clastic rock package of the Postmasburg Group (Beukes, 1986). The angular unconformity is directly overlain by a glacial tillite (Makganyene Diamictite) that forms the lowermost unit of the Postmasburg Group.

The Schmidtsdrif Subgroup forms the base of the Ghaap Group, and consists of upward-fining siliciclastic rocks representing subtidal to tidal-flat deposits that were subsequently drowned. Carbonate deposition, represented by the Campbellrand and correlative Malmani subgroup in both sub-basins, was established and developed into a major rimmed carbonate shelf on the Kaapvaal craton. The transition between the underlying carbonate build-up and the overlying BIF represented by Kuruman and correlative Penge BIFs is gradational (Fig. S8).

The Kuruman BIF in the Asbestos Hill Subgroup is sub-divided into two types: siderite-rich and Fe oxide-rich (Klein and Beukes, 1989). The former type consists of alternating siderite microbands and chert microbands. In addition to siderite and chert, minor minnesotaite, ankerite, and ferroan dolomite are present. The later type has similar textures and sedimentary structures to those in the siderite-rich BIF. The main difference is the mineralogical make up, with magnetite-rich IF having abundant magnetite in association with Fe-rich carbonates (siderite, ankerite, and/or ferroan dolomite) in the iron-rich mesobands. Hematite, stilpnomelane, and minnesotaite are minor components.

The depositional age of the Kuruman BIF is constrained by a SHRIMP U-Pb zircon age (2460 ± 5 Ma) of stilpnomelane-rich tuffaceous mudrocks within the upper part of the Kuruman BIF (Pickard, 2003) and a U-Pb zircon age (2521 ± 3 Ma) of a volcanic ash bed that crops out 40–50 m below the contact between the underlying Campbellrand Subgroup and the Kuruman BIF (Sumner and Bowring, 1996).

The Kuruman BIF is interpreted to represent shallowing-upwards deposition (initially in deep water) and is overlain by the Griquatown granular iron formation (GIF) that consists of lithofacies types deposited in a shallow epeiric sea. The GIF is typically composed of poorly sorted intraclastic and granular wackestone and packstone, with well-sorted grainstones not very common (Beukes and Gutzmer, 2008). Chert granules are common, but monomineralic greenalite, stilpnomelane, siderite, hematite, and magnetite granules and clasts are also present. Grains coated by hematite and magnetite, siderite, and/or Fe silicate are occasionally present. Granular bands in the Griquatown GIF have obviously been reworked by wave action because they often display wavy internal bedding similar to hummocky cross stratification formed by storm-wave action, suggesting that they were probably deposited in well-mixed and agitated environment above normal wave base.

The Koegas Subgroup is the uppermost unit of the Ghaap Group and represents the final stage of a long-term regressive period (Schröder et al., 2011). Rocks in this subgroup were deposited in foreshore to offshore environments of a prograding delta or submarine fan system. Immature arkosic wackes and subarkoses occur in proximal parts and pass to terrigenous mudstones and IF in offshore environments with low detrital input. Our IF samples were

from two drill cores: GTF01 and GEC01. The drill core GTF01, situated in the eastern part of the basin, represents a more proximal depositional setting associated with maximal sea level and the deposition of fine-grained and laminated IFs. The western GEC01 drill core comprises sediments from relatively deeper settings. The petrological and mineralogical composition of our samples is described in detail by Nel (2013). In most samples, dark green-black, very fine grained and massive Fe-silicate lutite (i.e., fine-grained cherty IF) layers alternate with lighter colored, greyish Fe-carbonate lutite layers. The abundance of Fe-oxides (mainly magnetite) is minor compared to Fe-silicates (stilpnomelane and greenalite) and Fe-carbonates (siderite and ankerite).

The Koegas Subgroup only develops in the deeper, southwestern part of the Griqualand West sub-basin. Its absence in the shallower parts, where the Griquatown GIF is directly overlain by the Makganyene diamictite, is explained by paleobathymetric considerations (Polteau et al., 2006). The transition from the upper Rooinekke Formation of the Koegas Subgroup to the overlying Makganyene Formation is transitional and 1 m-thick diamictite beds are commonly interbedded with the upper Rooinekke BIF. This feature, taken together with the presence of a glacial diamictite lens at the base of the Koegas Subgroup, indicates that there is a close environmental relationship between the Koegas Subgroup and the overlying Makganyene Formtion. The Makganyene Formation displays extreme thickness variations and contains a variety of rocks types including massive to coarsely bedded diamictites, sandstones, shales, BIFs, and stromatolite bioherms. The diamictite clasts consist essentially of chert, BIF, sandstone, and occasional carbonate sets in a fine ferruginous matrix. BIF clasts might be derived from the Asbestos Hills and/or Koegas subgroups. These rock-type associations depend on the exact location within the depositional basin (Polteau et al., 2006).

A tuffaceous turbidite unit separates the massive diamictites of the Makganyene Formation from the overlying Ongeluk Formation. The upper contact of the Ongeluk Formation basalts with the overlying Hotazel Formation is transitional over approximately 20 m and comprises hyaloclastites, black volcanic tuffs, and red jasper interbedded with diamictite and BIF (Polteau et al., 2006). Gumsley et al. (2017) documented a series of ID-TIMS U-Pb zircon ages for the basalts and related dolerite dikes and sills and obtained a weighted mean date of 2426 ± 3 Ma as the crystallization age of the Ongeluk Formation magmatism.

The Hotazel Formation is characterized by three Mn-ore layers, interlayered with magnetite-carbonate BIF. The BIF portions of the Hotazel succession are characterized by typically mm- to cm-scale laminated assemblages that are dominated by micro-crystalline quartz and magnetite in roughly equal model proportions (Thibon et al., 2019; Tsikos et al., 2010). Diagenetic carbonates (ankerite and calcite) constitute the next most important species in terms of model abundance, whereas Fe silicates (mainly greenalite, minnesotaite, and stilpnomelane) occur in much smaller modal amounts, suggesting only very shallow burial metamorphic overprint (below 200 °C) in the Hotazel sediments (Gutzmer and Beukes, 1996; Tsikos et al., 2003). The interbedded Mn-rich layers are dominated by variable relative proportions of very fine-grained braunite and hematite with a certain amount of manganiferous carbonate (kutnahorite and lesser manganoan calcite).

At the contact between the BIF and Mn bands, transitional lutites occur, ranging in thickness from a few decimeters up to several meters (Gutzmer and Beukes, 1996; Lantink et al., 2018; Tsikos et al., 2003, 2010). These lutites are rich in hematite and Mn-carbonates and also contain some magnetite disseminations.

A conformable and usually gradational contact separates the Hotazel Formation from the overlying Mooidraai Formation comprising Fe-bearing limestone and dolomite. A carbonate Pb-Pb age of 2394 ± 26 Ma has been obtained from a dolomitized portion of the Mooidraai Formation (Bau et al., 1999).

The Duitschland Formation is the basal formation of the Pretoria Group of the Transvaal Supergroup. It unconformably overlies both the Tongwane Formation and the Penge IF and is unconformably overlain by the Timeball Hill Formation in the Duitschland area (Bekker et al., 2001). The Duitschland Formation is a mixed sedimentary succession which consists of conglomerate, glacial diamictites, mudstones, marls, siltstones, quartzites, and stromatolitic and non-stromatolitic limestones and dolostones (Warke and Schröder, 2018). The ∼ 1000 m thick Duitschland Formation is divided into lower and upper parts which are separated by the MID-Duitschland Unconformity (MDU). The lower Duitschland Formation is composed of a basal chert conglomerate which is overlain by a 30–200 m thick glacial diamictite. Overlying the diamictite are two upward coarsening cycles of mudstones to medium-grained sandstones, with minor limestones, limestone slump breccias, and stromatolitic dolostones deposited during delta progradation (Coetzee, 2001). The Duitschland Formation has been interpreted to be deposited either in a lacustrine (Eriksson and Catuneanu, 2004) or a shallow marine environment (Bekker et al., 2001). The depositional age of the Duitschland Formation is constrained to between ∼ 2480 and ∼ 2310 Ma based on dates obtained from the underlying Penge IF and the overlying Timeball Hill Formation, respectively (Hannah et al., 2004; Nelson et al., 1999; Rasmussen et al., 2013a). Detrital zircon geochronology suggests a maximum depositional age of 2424 ± 12 Ma for the upper Duitschland Formation (Schröder et al., 2016).

The disappearance of the mass independent fractionation of sulfur (MIF-S) signal was preserved in both the Duitschland Formation and the Rooihoogte Formation of the Transvaal Supergroup (Guo et al., 2009; Luo et al., 2016; Izon et al., 2022). If the two formations are not correlative, it might indicate oscillation between MIF-S and non-MIF-S conditions (Gumsley et al., 2017). However, based on litho-, sequence-, and chemostratigraphic similarities (Coetzee, 2001; Luo et al., 2016; Warke and Schröder, 2018), the Duitschland Formation might be correlative to the Rooihoogte Formation, suggesting that the disappearance of the MIF-S signal was a secular, unidirectional change.

The Timeball Hill Formation conformably overlies the Rooihoogte Formation and represents a deltaic to shallow-marine succession (Dorland, 1999). The lower part of the Timeball Hill Formation is composed of a black, finely laminated carbonaceous shale, which coarsens upwards into either quartzite or oolitic ironstone. The oolitic units then fine upwards into finely laminated carbonaceous shale. Locally a diamictite layer is developed along the top of the Timeball Hill Formation. The Timeball Hill oolitic ironstone beds cover an area of > 100,000 km^2.

These ironstones are hosted in siliciclastic lithologies ranging from highly mature orthoquartzites, siltstones, to claystones. There are three types of oolitic ironstones. The first type is characterized by tightly packed oolites with uniform concentrically laminated cortices and some hematite-coated quartz grains set in a dense, very fine-grained matrix of dusty hematite and Fe-rich chlorite. The second type is marked by the distribution of hematite oolites with variable cortex textures in a quartzite host and consists predominantly of hematite with some chlorite. The third type is composed of hematite with minor siliciclastic material. The oolites consist of remarkably even, concentric cortices on a microscopic scale.

A Re-Os age of 2316 ± 7 Ma for synsedimentary to early diagenetic pyrite (Hannah et al., 2004) and a U-Pb age of 2309 ± 9 Ma for tuff in the lower Timeball Hill Formation (Rasmussen et al., 2013a) provide constraints on the depositional age of the Timeball Hill ironstones.

3. Methods

Iron formation and ironstone samples have been petrographically analyzed using scanning electron and reflected light microscopy (e.g., Beukes and Gutzmer, 2008; Wang et al., 2017) and suitable representative samples were selected for further elemental and isotopic analyses. Our sample set is composed of GIF and BIF. Nearly all of the samples were taken from Fe oxide-rich sections with low levels of detrital siliciclastic and volcanoclastic material. We have avoided samples from sequences that have experienced obvious secondary ore-forming processes (e.g., supergene and hydrothermal Fe-enrichment). Samples with visible signs of fluid flow (extensive veining, disruption of sedimentary, and mineral phases cross-cutting sedimentary layers) were also avoided. Note that a bulk sample approach is used to provide an estimate of the average chemical composition of IF, rather than distinct mineral phases. Sample details including the dominant Fe mineralogy of each sample and relevant references are listed in Table S1.

3.1. Elemental concentration analyses

Bulk rock samples were cut with a diamond edge rock saw to remove weathered surfaces, and subsequently crushed in an agate mill to a fine powder. Approximately 50 mg of sample powder was dissolved in Teflon beakers using concentrated HF and HNO_3 for 24 h at 100 °C, dried down, and subsequently dissolved again using Aqua Regia at a ratio of 1 part HNO_3 to 3 parts HCl for 48 h at 120 °C before being dried down. In the event that undigested powder remained after the Aqua Regia digestions, samples were centrifuged to remove insoluble residue and the supernatant was carefully transferred into Teflon beakers and dried down. Final residues were dissolved in 5 ml 6 N HCl for stock solutions for geochemical analyses.

A small aliquot ($\sim$10 µl) of the 5 ml 6 N HCl stock solution was then dried down and brought up in 4 ml of 5 % HNO_3 containing an internal spike of 1 ppb Indium. The resulting solutions were analyzed in the Department of Earth and Planetary Sciences at Yale University by inductively coupled plasma mass spectrometry (ICP-MS; ThermoFisher Scientific Element XR) to determine selected major and trace element (including rare earth element, REE) concentrations using a standard sample introduction system. Measurement precision was generally better than 5 % (2σ) for these elements. The data from United States Geological Survey (USGS) geostandards BHVO-2 and NOD-A-1 processed along with samples during each analytical run were within 5 % of reported values.

To account for possible sedimentary Gd enrichment due to seawater scavenging processes, shale-normalized europium (Eu/Eu*) anomalies reported here are calculated based on the equations of Bau and Dulski (1996), as follows:

$$Eu/Eu* = [Eu/Eu_{(PAAS)}]/[0.67 \times (Sm/Sm_{(PAAS)}) + 0.33 \times (Tb/Tb)_{(PAAS)}]$$

where PAAS refers to the post-Archean Australian Shale composite (McLennan, 1989).

3.2. Iron isotope analyses

Sample solutions prepared for bulk rock geochemical analyses were subsequently used for Fe isotope analyses. Samples were purified by ion-exchange chromatography with AG-MP-1 M resin (100–200 mesh; methods modified from Asael et al., 2013). The resin was preconditioned in a HCl medium by running 18.2 MΩ-cm H_2O, 0.24 N HCl, 0.5 N HNO_3, and 7 N HCl through the column. Sample solutions containing 8 µg Fe were dried down and dissolved with 1 ml 7 N HCl + 0.001 % H_2O_2 prior to ion-exchange

chromatography. After samples were loaded on the column, matrix elements were eluted with 7 N HCl, while Fe(III) remained strongly adsorbed on the resin and was quantitatively retained. Iron was subsequently eluted with 2 N HCl and 0.5 N HNO_3, with a procedural yield of > 97 %. Iron isotopes were measured using a Thermo-Fisher Scientific Neptune Plus Multi-Collector ICP-MS (MC-ICP-MS) at the Yale Metal Geochemistry Center. Iron isotope results were bracketed by, and are reported in standard delta notation in per mil (‰) values, relative to the IRMM-14 standard, as:

$$\delta^{56}Fe = [(^{56}Fe/^{54}Fe)_{sample}/(^{56}Fe/^{54}Fe)_{standard} - 1] \times 1000$$

The total procedural Fe blank was<40 ng, which is negligible relative to the amount of Fe in the samples. Analytical accuracy and precision of measured $\delta^{56}Fe$ values were assessed by repeated processing and analysis of the USGS reference material BHVO-2 and NOD-A-1 as unknowns alongside samples. The average internal sample standard error (2σ) was 0.02 ‰. Measured $\delta^{56}Fe$ values were 0.11 ± 0.14 ‰ (n = 40) for BHVO-2 and −0.30 ± 0.15 ‰ (n = 40) for NOD-A-1, which are within error of previously published values for these two standards (Dideriksen et al., 2006; Millet et al., 2012). In addition to the standards, three unknown samples were processed in duplicate and all agree with the original analyses with 2σ values < 0.03 ‰.

4. Results

Here, we present a detailed record of bulk-rock Fe isotopes and Mn/Fe ratios from Archean to early Paleoproterozoic IFs and ironstones in order to explore the redox dynamics of the early Earth (Fig. 1 and Table S1-S2). Data derived from $\sim$ 759 individual samples include both new results (n = 247) and those obtained from a comprehensive literature survey (n = 512). Briefly, the measured
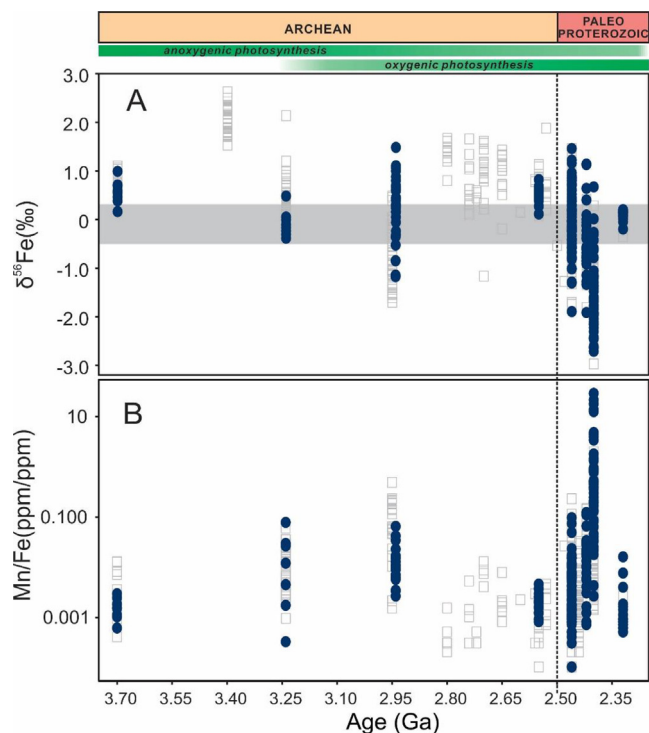

Fig. 1. Temporal variations in $\delta^{56}Fe$ values (A) and Mn/Fe ratios (B) of bulk Archean and early Paleoproterozoic IFs. Filled blue circles represent new results; unfilled gray squares indicate previous results. Detailed sources of these data are provided in the *Supplementary Materials*. Sample standard error is smaller than the data points. Horizontal gray bar denotes the range of $\delta^{56}Fe$ values of lithogenic and hydrothermal Fe(II) sources (−0.5 < $\delta^{56}Fe$ < 0.3 ‰) (Beard et al., 2003; Johnson et al., 2020; Severmann et al., 2004). Note the logarithmic scale in (B).

δ^{56}Fe values of samples studied here span a large range from -2.98 ‰ to up to $+2.63$ ‰, but the majority of samples, especially those from the Archean, are characterized by positive δ^{56}Fe values. The Mn/Fe ratios of these IF samples also show a broad range, with the highest Mn concentrations accompanied by the lightest Fe isotope compositions observed in samples from the ~ 2.4 Ga Hotazel Formation.

5. Discussion

5.1. Evaluation of detrital contamination and post-depositional alteration

Iron formations can have complex sedimentary and post-depositional histories. In order to interpret the temporal changes in IF δ^{56}Fe values and Mn/Fe ratios as variations in primary geochemical compositions, it is important to consider the possible effects of detrital contamination and post-depositional (diagenetic, hydrothermal, and metamorphic) alteration on the studied IF samples. Nearly all samples have a negligible detrital component (< 0.5 wt% Al_2O_3) and there exists no significant negative correlation between the paleoredox data (δ^{56}Fe values and Mn/Fe ratios) and detrital indicators (e.g., Al_2O_3 and TiO_2, Table S3), suggesting that secular variations in redox indicators were not driven by the dilution of authigenic components by detrital input. Dissimilatory microbial Fe reduction (DIR) is a common diagenetic process during diagenesis, whereby microbial organisms use organic carbon as an electron donor to reduce Fe(III). This has been shown to lead to Fe isotope fractionations of up to ~ 3 ‰, releasing Fe(II) enriched in the light isotopes and leaving residual oxides with positive δ^{56}Fe values (Beard et al., 1999; Crosby et al., 2005, 2007; Icopini et al., 2004). Numerical modelling has been used to argue that the maximum net change in bulk rock δ^{56}Fe values resulting from diagenetic Fe cycling is likely < 1 ‰ (Kunzmann et al., 2017). While this mechanism may hypothetically explain positive δ^{56}Fe values of sedimentary rocks with low authigenic Fe enrichment (Gibson et al., 2020), this process is unlikely to significantly affect the bulk Fe isotope composition of rocks where Fe is the dominant geochemical component. Further, even though DIR is highly efficient, it is likely that only a small part of Fe(II) would be lost back to the water column because a large fraction would be absorbed onto Fe(III) oxyhydroxides or precipitated as mixed valence iron-bearing minerals in the sedimentary pile (Aller et al., 2004; Planavsky et al., 2012), thus not significantly altering the whole-rock Fe isotope composition of iron-rich sediments. Given that the mineralogy of our samples (with the exception of the ~ 2.31 Ga Timeball Hill ironstone) is commonly characterized by large amounts of mixed valence Fe oxides, and the flux of reactive iron oxides would have been greater than the input of organic matter, it is unlikely that DIR would have greatly affected the Fe isotope composition of bulk sediments, especially the extremely organic matter-poor, oxide-dominated IFs (Planavsky et al., 2012).

Iron formations are considered to be resistant to the overprinting of their Fe isotope signatures by hydrothermal and metamorphic processes (Sun et al., 2018) and are therefore robust archives of Fe isotope signatures. High temperature processes do not tend to lead to strong fractionations in the Fe isotope system (Johnson et al., 2020). There is also no evidence for a strong hydrothermal overprint on the Fe texture of the studied IFs, with either banded or granular textures well preserved and a lack of fractures and veins. A hydrothermal control on Fe isotope composition is also not supported by the trace element characteristics of these IFs. Among the REE, Eu is redox sensitive, and positive Eu anomalies in IFs (Fig. 2) commonly indicate a high-temperature hydrothermal influence on IF genesis (Bau and Dulski, 1996). Given
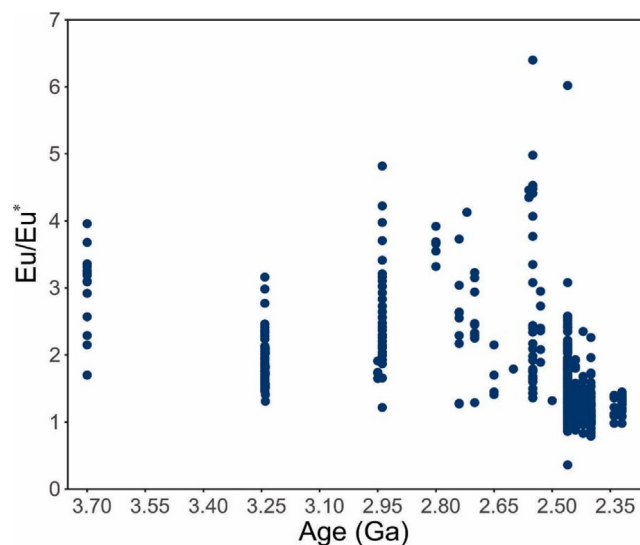

Fig. 2. Temporal variation in the PAAS-normalized Eu anomalies of the Archean and early Paleoproterozoic IFs including data from this and previous studies. Detailed sources of these data are provided in the *Supplementary Materials*. PAAS: post-Archean Average Australia Shale composite after McLennan (1989).

that Eu(III) can be reduced to Eu(II), Eu in particular appears to be sensitive to remobilization under reducing conditions and at elevated temperatures (Bau and Dulski, 1996). In the diagram of Eu versus neighboring REE, any deviation from a linear trend would indicate anomalous behavior of Eu. However, there is a strongly positive relationship between Sm and Eu for our samples (e.g., $R^2 = 0.96$ for the Moodies BIF samples), suggesting insignificant effects from either detrital contamination or leaching during post-depositional alteration on Eu (Bolhar et al., 2015), although the La-Ce geochronology revealed post-depositional light REE mobility in the Moodies BIF (Bonnand et al., 2020). Furthermore, the absence of a correlation between Eu anomalies and δ^{56}Fe values, coupled with the presence of a relationship between Mn/Fe ratios and δ^{56}Fe values (see discussion 5.3 below), in our samples indicates that the Fe isotope composition is more likely related to the degree of Fe oxidation rather than varying degrees of hydrothermal input.

All IFs have experienced a certain degree of metamorphism, by which process the Fe isotopes may be redistributed by either diffusion or mineral reactions. Diffusional rates and spatial scales suggest that the primary millimeter- and micrometer-scale Fe isotope heterogeneity that may have resulted from either the deposition or early diagenesis of Fe-rich sediments (Steinhoefel et al., 2009) might be erased by the effects of regional metamorphism (Czaja et al., 2013; Li et al., 2013). However, the bulk Fe isotope compositions are expected to still be reflective of those of the original Fe-rich sediments. Dauphas et al. (2004, 2007) reported generally positive Fe isotope data for high-grade (up to granulite facies) banded rocks from Greenland and Canada, and interpreted these values as a consequence of low-temperature processes involving transport, oxidation, and precipitation of Fe, suggesting that metamorphism did not affect the bulk Fe isotope compositions. Frost et al. (2007) concluded that the isotopic compositions of the ca. 1880 Ma Biwabik iron formation magnetite were not changed during contact metamorphism relative to their pre-metamorphic compositions. By contrast, Valaas-Hyslop et al. (2008) argued that δ^{56}Fe values in the metamorphosed Biwabik iron formation were 0.3 ‰ lower than those in their protolith and concluded that metamorphism decreases the δ^{56}Fe values in rocks containing iron silicates. In any case, the positive δ^{56}Fe values in IFs cannot be explained by metamorphic reactions. The pristine

preservation of fine-scale lamination and textures within the Fe-ooids of the studied GIF and BIF samples further argues against the influence of texturally destructive metamorphism. Therefore, we can be reasonably confident that the bulk Fe isotopic compositions are likely to be primary in nature.

5.2. Primary iron mineralogy

Determining the dominant primary Fe mineralogy of IFs is key to deciphering their redox implications. The notion that the Fe(III) minerals (i.e., hematite precursors) are the primary phase for IF was suggested over four decades ago (Ayres, 1972) and many time since (Ahn and Buseck, 1990; Beukes and Gutzmer, 2008; Pecoits et al., 2009; Robbins et al., 2019; Sun et al., 2015; Trendall and Blockley, 1970). Given that Si concentrations in Precambrian seawater are estimated to have been high (~1 to 2 mM), assuming controlled by the solubility of amorphous Si and sorption to silicate minerals (Maliva et al., 2005), primary Fe(III) minerals should be enriched in Si, perhaps akin to an Fe(III)-Si gel. Previous Fe(II) oxidation experiments in the presence of dissolved Si (Percak-Dennett et al., 2011; Wu et al., 2012) along with spectroscopic (Doelsch et al., 2001; Doelsch et al., 2002; Doelsch et al., 2003) and Si isotope studies (Reddy et al., 2016; Zheng et al., 2016), suggest that the primary Fe(III) precipitate in IFs was an Fe(III)-Si gel. However, recent Fe oxidation experiments with marine phototrophic Fe(II)-oxidizing bacteria under simulated Archean ocean conditions indicate that some fraction of the primary Fe(III) and Si phases become separated during deposition because of the competing effects of organic carbon (Schad et al., 2019). A full understanding of how much of the precipitated Fe(III) and Si are in the form of an Fe(III)-Si gel or separate ferrihydrite and amorphous Si phases requires further experimental study.

Alternatively to Fe(III) oxyhydroxides, the primary mineral phase of IFs has also been suggested to be dominantly Fe(II) or mixed valence phases, such as greenalite or various "green-rust" phases. Greenalite has been identified in chert layers from several Paleoproterozoic and Archean IFs (e.g., Muhling and Rasmussen, 2020; Rasmussen et al., 2017). The identification of fine-grained greenalite nanoparticles in laminated cherts has been taken as evidence for water column precipitation of this mineral (Rasmussen et al., 2013b), supported by experimental evidence for greenalite precipitation (Tosca et al., 2016). Muhling and Rasmussen (2020) suggest that the greenalite nanoparticles are formed in hydrothermal vent plumes before being distributed throughout the oceans and being deposited. However, in such a scenario, the greenalite nanoparticles would be precipitated in vent fluids distal to the depositional setting of many IFs (e.g., stable continental shelf) during initial mixing of vent fluids and ambient seawater, essentially forming in disequilibrium. Transport to other depositional centres (e.g., shelf slope, continental shelf) would then make these greenalite particles allochthonous, decoupling their chemical precipitation from that of IFs. Such an interpretation would account for the petrographic features of greenalite nanoparticles and their widespread depositional nature, while simultaneously decoupling the implications of their chemical precipitation from those of the bulk ocean.

In contrast with a generally proposed primary origin of hematite via dehydration of original Fe(III) oxyhydroxides, Rasmussen et al. (2014) attributed the formation of hematite to the oxidation of primary greenalite by post-depositional heating (>200–400 ℃) and O_2-bearing groundwater. If correct, the original Fe isotope composition of Fe-rich sediments should be close to 0 ‰, because in the absence of fractionation involved with redox transformations (Konhauser et al., 2017; Johnson et al., 2020), primary Fe(II)-silicate phases (such as greenalite) would have an Fe isotopic

signature close to that of the seawater dissolved Fe(II). These Fe isotope values are also unlikely to have been strongly affected by post-depositional processes under oxidizing conditions, because Fe(III) solubility is low at circum-neutral pH (Dauphas and Rouxel, 2006). Further, secondary oxidation of greenalite cannot produce the commonly positive $\delta^{56}Fe$ values observed in our samples (Johnson et al., 2022), given that it requires high fluid/rock ratios. Such high water to rock ratios would be expected to result in either near-complete removal of Fe from the rock or alteration of REE patterns in IFs (Bau, 1993); yet, many IFs retain seawater-like REE patterns despite early diagenesis and subsequent metamorphism (Planavsky et al., 2010). Additionally, such an interpretation is in conflict with the very low oxygen isotope features of hematite in the Dales Gorge Member (Li et al., 2013), which requires a very low temperature of formation. Further, Fe(II) silicate precipitation requires pH conditions of 7.75–8.3 (Tosca et al., 2016), which are at odds with those predicted for Archean seawater (e.g., 6.5–7.0; Halevy and Bachan, 2017). Finally, the predominance of Fe(III) phases on a basin scale is difficult to explain via post-depositional oxidation of Fe(II) silicates driven by groundwater flow on reasonable time scales (Robbins et al., 2019), supporting the interpretation that Fe(III)-oxyhydroxides should be the dominant primary phase for IFs.

Nevertheless, despite the evidence above precluding a primary origin of greenalite, previous important petrographic features, such as greenalite nanoparticles (Rasmussen et al., 2013b), and results of recent Fe cycling experiments (Schad et al., 2022), cannot be well explained. Therefore, it remains possible that both greenalite and Fe(III)-oxyhydroxide were primary IF mineral phases, with one dominant over the other at various times (e.g., before and after the GOE) and in different depositional settings (e.g., deep water vs shallow water). Regardless, from an Fe isotope perspective, in contrast with those $\delta^{56}Fe$ values (-0.78 ~ -0.1 ‰) measured for greenalite in IFs (Frost et al., 2007), the predominance of positively fractionated Fe isotope values in nearly all IFs—using a standard framework for interpreting Fe isotope values—provides strong support for genetic models that invoke precipitation of primary Fe(III)-oxyhydroxide minerals (Rouxel et al., 2005; Dauphas et al., 2017).

Carbonated green-rust has been observed in modern ferruginous and sulfate-poor lake (Zegeye et al., 2012). It is possible that green-rust was a precursor to magnetite in IFs, as supported by thermodynamic calculations and precipitation experiments (Halevy et al., 2017; Li et al., 2017). However, green-rust may have be oxidized by anoxygenic phototrophic Fe(II)-oxidizing bacteria in ancient oceans (Han et al., 2020) and the positive $\delta^{56}Fe$ values of IFs cannot be explained using the $^{56}Fe/^{54}Fe$ fractionation of ca. −0.2 ‰ between Fe(II) and green-rust (Wiesli et al., 2004). Therefore, we suggest that green-rust is not the dominant precursor precipitate for IFs and that IF Fe isotope systematics are consistent with oxidation of Fe(II) and the subsequent deposition of Fe(III)-oxyhydroxide as IFs. Secular variation in Fe isotope and Mn enrichment data may therefore present a valuable tool for tracking changes in the relative importance of the mechanisms underlying marine Fe(II) oxidation.

5.3. Tracking iron oxidation through time

Most Archean IFs (>2.5 Ga) are characterized by highly positive $\delta^{56}Fe$ values (Fig. 1A), suggesting that these IFs are the product of the partial oxidation of Fe(II) and a relatively large marine reservoir of aqueous Fe(II) (Rouxel et al., 2005). The low Mn/Fe ratios (<0.01) (Fig. 1B) of these IFs suggest that while partial Fe(II) oxidation was common, Mn(II) oxidation and transport to the sediment pile was insignificant (Kurzweil et al., 2016). For these Archean IFs, no clear relationship between $\delta^{56}Fe$ values and Mn/Fe ratios exists (Fig. 3A-C), further suggesting a paucity of free O_2 in the water column.
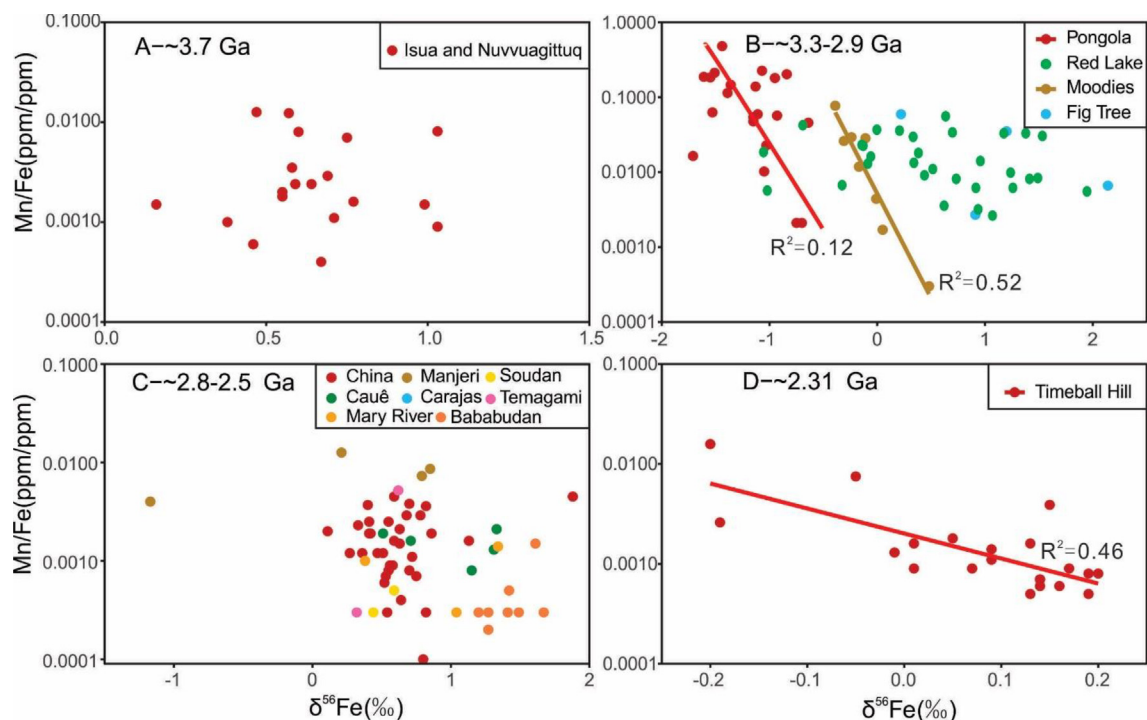
Fig. 3. Relationships between $\delta^{56}Fe$ values and Mn/Fe ratios for IFs across the different ages. Data from this and previous studies. Detailed sources of these data are provided in the *Supplementary Materials*.

These data are supportive of deposition in an anoxic ocean–atmosphere system, consistent with evidence from the sedimentary record of the MIF-S—the prevailing geochemical index for an anoxic atmosphere (Farquhar et al., 2011). Under these conditions, photoferrotrophs would have been the dominant force in driving Fe(II) oxidation (Czaja et al., 2013).

It should be noted, however, that some IFs deposited between 3.3 and 2.8 Ga are characterized by lower $\delta^{56}Fe$ values (Fig. 1A), suggesting a greater degree of Fe(II) oxidation. In conjunction with their higher Mn/Fe ratios, we suggest that this Fe(II) oxidation correlates with the emergence and/or increased impact of oxygenic photosynthesis. There is appreciable scatter in the paleoredox data for these units, yet the data from ∼ 3.2 Ga Moodies IF in the Barberton greenstone belt (Heubeck, 2019) and ∼ 2.95 Ga Sinqeni IF (Planavsky et al., 2014) in the lower Mozaan Group feature a significant negative correlation between Mn/Fe ratios and $\delta^{56}Fe$ values (Fig. 3B), supporting the interpretation that O_2 began to accumulate in shallow-marine settings before ∼ 3.2 Ga, allowing for Mn (II) and Fe(II) oxidation during deposition. Given that this period predates the permanent accumulation of atmospheric O_2 during the GOE, as indicated by the record of MIF-S (Farquhar et al., 2011), this suggests that the O_2 was sourced from local production of marine cyanobacteria. These oxygenated shallow seawater oases are expected to be transient and spatially restricted in nature.

This spatial variation in shallow seawater O_2 levels is supported by the common co-occurrence of highly positive $\delta^{56}Fe$ values and low Mn/Fe ratios (<0.01) within other IFs of similar ages (Busigny et al., 2017; Planavsky et al., 2012) and by the shallow-water Nconga GIF in the upper Mozaan Group (Smith et al., 2017). This GIF possesses positive $\delta^{56}Fe$ values and low Mn/Fe ratios (<0.01) (Smith et al., 2017). Biogenic textures in the granules of this GIF are considered to reflect some of the earliest evidence for shallow-water biological Fe oxidation (Smith et al., 2020); these may represent fossil photoferrotrophs given their formation in the photic zone. The contribution of cyanobacteria and other O_2-dependent Fe(II)-oxidizers (i.e., microaerophilic and nitrate-

reducing bacteria) to Fe(II) oxidation may have been hindered by a shallow redoxcline during this time (Homann et al., 2018; Ossa Ossa et al., 2019). This would allow photoferrotrophs a preferential access to upwelling nutrients below the redoxcline, owing to their adaption to lower light levels (Kappler et al., 2005), thus limiting the productivity of cyanobacteria in the surface ocean (Jones et al., 2015) and restricting cyanobacteria to very nearshore environments where there may have been nutrient input from emergent continents. Further, cyanobacterial activity would have been further curtailed by the high Fe(II) concentrations of the anoxic oceans during this time, as recorded by highly positive Eu anomalies, a high-temperature hydrothermal indicator of Fe input (Konhauser et al., 2017), observed in IFs of this age (Fig. 2), because upwelling ferruginous seawater would lead to oxidative stress resulting from reactions between Fe(II) and O_2 (Swanner et al., 2015). Overall, the IF record points towards an Archean paleoredox landscape prior to 2.5 Ga in which cyanobacteria are ecologically restricted and photoferrotrophs largely drive IF deposition, outside of oxygen oases where local O_2 production is elevated.

Following this time, there are substantial shifts in the $\delta^{56}Fe$ values and Mn/Fe ratios of ∼ 2.5–2.4 Ga IFs (Fig. 1), which we interpret to reflect changing marine redox conditions across large portions of the continental margins. Specifically, as $\delta^{56}Fe$ values in IFs become more negative towards ∼ 2.4 Ga (Czaja et al., 2018; Heard and Dauphas, 2020), Mn/Fe ratios become higher (Fig. 4 and S1), with negative correlations between Mn/Fe ratios and $\delta^{56}Fe$ values observed for all IF samples of this interval (Fig. 5 and S9). We suggest that this is the product of gradually increasing seawater O_2 levels availability throughout this stage, whereby the negative $\delta^{56}Fe$ values are linked to a progressive distillation during the drawdown of the Fe(II) reservoir (Kurzweil et al., 2016; Rouxel et al., 2005). Microbial Fe reduction of continentally sourced Fe(III)-bearing minerals—which can preferentially release light Fe isotopes to seawater—may have also contributed to this isotopically depleted Fe(II) reservoir (Severmann et al., 2008; Li et al., 2015). In either case, these Fe isotope data are compatible
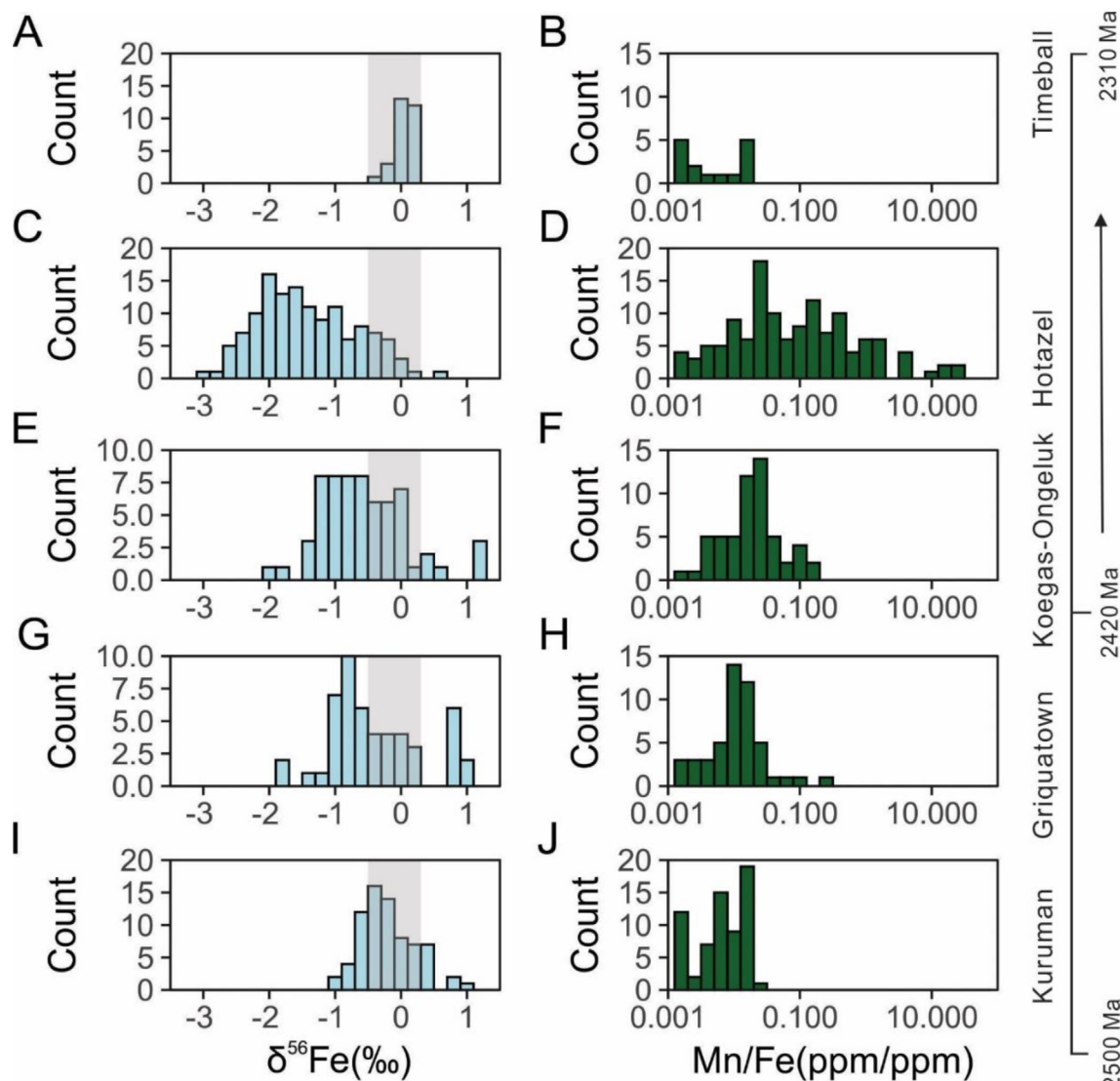
Fig. 4. Temporal variation of δ^{56}Fe values and Mn/Fe ratios of IFs in the Transvaal Supergroup. Data from this and previous studies. Detailed sources of these data are provided in the *Supplementary Materials*. Vertical gray field denotes the range of δ^{56}Fe values of lithogenic and hydrothermal Fe(II) sources ($-0.5 < \delta^{56}$Fe < 0.3 ‰) (Beard et al., 2003; Johnson et al., 2020; Severmann et al., 2004).

with a scenario in which near-complete Fe(II) oxidation is occurring at the redox boundary of a stratified water column (Busigny et al., 2014). This suggests that substantial O_2 had started to accumulate in the surface ocean, permitting the development of a stable redoxcline separating deep anoxic and shallow oxygenated seawater. This is consistent with an increasingly important role of O_2-mediated Fe(II) oxidation. This relationship between IF δ^{56}Fe values and Mn/Fe ratios also adds to our understanding of the importance of the Fe(III) oxide sink during this time, and supports the inference that partial Fe(II) oxidation played an important role in driving the Fe isotopic signature of Fe-bearing sediments during the Archean–Paleoproterozoic (e.g., Rouxel et al., 2005). This is in agreement with recent triple Fe isotope evidence which demonstrates that the oceans would have been characterized by a significant oxidized Fe sink during this time (Heard et al., 2020).

There is also a decline in the magnitude of positive Eu anomalies (Fig. 2) for IF samples of this interval. When combined with increasing Fe(II) oxidation, waning hydrothermal Fe input could have contributed to falling Fe(II) levels in seawater, which in turn, would have alleviated Fe toxicity issues that cyanobacteria may

have faced (Swanner et al., 2015). Collectively, these events would accelerate the expansion and proliferation of cyanobacteria (Jones et al., 2015), finally giving rise to well-oxygenated surface seawater. Greater O_2 availability could also have benefited other O_2-dependent Fe(II)-oxidizers. Further, a progressive and pervasively oxygenated surface seawater layer would also imply some degree of free O_2 accumulation in the atmosphere assuming gas–water exchange equilibrium. A degree of atmospheric oxygenation during this time would be consistent with geochemical proxy records for oxidative weathering (e.g., chromium abundance) in rocks since ~ 2.5 Ga (Konhauser et al., 2011). It is worth noting is that the sulfur isotope record of the Hamersley and Eastern Transvaal basins oscillate between values indicative of mass independent and dependent fractionations during this interval (Fig. S6 and S8) (Philippot et al., 2018; Poulton et al., 2021; Warke et al., 2020).

While IFs are rare between 2.4 and 2.3 Ga, shallow marine GIFs with low Mn/Fe ratios were still deposited. This may reflect a transition from Fe-Mn-rich to Fe-Mn-poor oceans. This could be linked to the large-scale oxidative drawdown of the marine Fe(II) and Mn(II) reservoir as evidenced by the burial of the giant 2.5–2.4 Ga IF and Mn deposits of South Africa and Western Australia, and Fe iso-

tope systematics indicative of Rayleigh fractionation of a significantly diminished Fe(II) pool at the end of ~ 2.4 Ga. Alternatively, this could potentially be related to waning hydrothermal Fe(II) input, which would be supported by the diminished Eu anomalies of the GIFs of this age (Fig. 2). Unlike older IFs, these units display a narrow and restricted range of δ^{56}Fe values, which are indistinguishable from those of lithogenic and hydrothermal Fe(II) sources (−0.5 < δ^{56}Fe < 0.3 ‰) (Beard et al., 2003; Johnson et al., 2020; Severmann et al., 2004). This observation is an expected consequence of essentially quantitative Fe(II) oxidation within oxic surface waters in gas exchange equilibrium with an oxygenated atmosphere, consistent with other independent estimates for high atmospheric pO$_2$ (Bekker and Holland, 2012).

5.4. Modeling ocean–atmosphere O$_2$ abundance

Assuming that O$_2$-mediated Fe(II) oxidation occurred in the surface oceans, most likely the photic zone, we can use an Fe(II) oxidation model to convert Fe isotope values into quantitative estimates for the dissolved O$_2$ concentrations of shallow seawater (Czaja et al., 2012, 2013; Wang et al., 2022). This approach is most directly applicable to shallow-marine GIFs and ironstones (Wang et al., 2022), which feature Fe coated grains. In contrast to BIFs deposited below storm-wave base, these facies were deposited in water depths close to, or above, storm-wave base in near-shore environments (Bekker et al., 2010; Konhauser et al., 2017). This is important because unlike deep-marine settings, shallow seawater is unlikely to be deficient in dissolved O$_2$ relative to the overlying oxygenated atmosphere (e.g., Reinhard et al., 2016; Wang et al., 2022). The first appearance of GIFs in the geological record is

marked by the ~ 2.95 Ga Nconga Formation and is followed by the ~ 2.45 Ga Griquatown and ~ 2.31 Ga Timeball Hill formations, the latter two spanning a critical interval pertinent to the GOE. The Fe isotope composition of these facies show a progression through time from positive δ^{56}Fe values, to a mixture of both positive and negative values, and ultimately to values within a narrow range relative to bulk silicate Earth (Fig. 1A). Therefore, these units record a transition from restricted to more widespread partial Fe(II) oxidation in the Archean oceans, followed by quantitative Fe(II) oxidation in shallow seawater between 2.45 and 2.31 Ga. Based upon the linked Mn/Fe and Fe isotope records of these GIFs, we suggest that this transition was caused by an increase in the availability of O$_2$ in the surface oceans and atmosphere.

Assuming that surface waters were close to gas exchange equilibrium with the overlying atmosphere (e.g., Wang et al., 2022), Fe isotope evidence for partial Fe(II) oxidation in shallow seawater points towards low atmospheric pO$_2$, whereas quantitative Fe(II) oxidation requires comparatively higher pO$_2$. Although a dispersion-reaction model has been applied previously to describe the Fe(II) oxidation of Archean BIFs deposited prior to the oxygenation of the atmosphere (Czaja et al., 2013), this model is not applicable to IFs deposited under higher dissolved O$_2$ conditions (>0.01 µmol/kg), and is difficult to reconcile with BIFs with negative Fe isotopes (Johnson et al., 2020). As such, we follow the approach of Wang et al. (2022) and use a Rayleigh distillation model because IFs deposited in the oases described above possess a much greater spread in Fe isotope compositions (Fig. 1). We suggest that this is best explained by the ongoing removal of isotopically heavy Fe (as Fe(III) oxyhydroxides) via the progressive partial oxidation of a seawater Fe(II) reservoir (i.e., Rayleigh distillation) (e.g., Rouxel
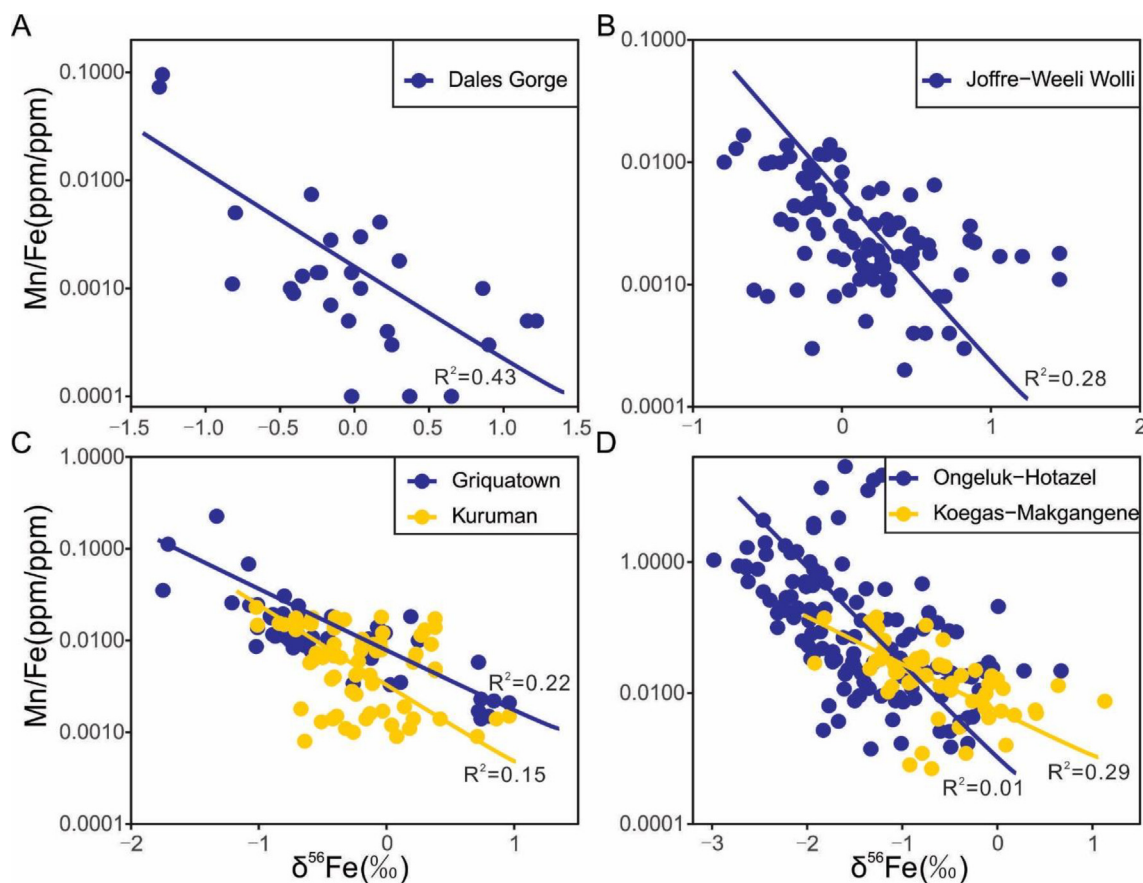

Fig. 5. Relationships between δ^{56}Fe values and Mn/Fe ratios of IFs in the Hamersley Group (A-B) and Transvaal Supergroup (C-D). Data from this and previous studies. Detailed sources of these data are provided in the *Supplementary Materials*.

et al., 2005). This interpretation is supported by the observed negative correlations between δ^{56}Fe values and Mn enrichments (Figs. 3 and 5), which shows that the Fe isotopic trends are related to the extent of oxidation (Kurzweil et al., 2016). The Rayleigh fractionation model calculates the Fe isotopic composition of the reactant pool, as well as the instantaneous and cumulative oxidation products for oxidation extents between 1 and 99 % of the input pool. Isotopically, the input pool is constrained to fall between crustal and hydrothermal values for Fe (-0.5 < δ^{56}Fe$_{in}$ < +0.3 ‰) (Beard et al., 2003; Johnson et al., 2020; Severmann et al., 2004). If an observed isotope value is ^{56}Fe-enriched relative to the range of likely input values, we use the Rayleigh model for a cumulative product. However, some IF samples feature negative δ^{56}Fe values, requiring separation of distinct Fe pools during fractionation. As such, if an observed isotope value is ^{56}Fe-depleted relative to this range of input values, we use the Rayleigh model for an instantaneous product. If an observed isotope value falls within the range of possible input values—it is not fed into the model at all, it is taken as indistinguishable from quantitative Fe(II) oxidation. The fraction of Fe(II) oxidation determined from the inversion of the Rayleigh distillation model is then compared to results from the kinetic Fe(II) oxidation model that calculates the amount of Fe fractionation based on a stochastic sampling of input parameters including temperature, pH, and the residence time for a mixed layer depth of either 50 or 90 m (Wang et al., 2022). The stochastic model for oxidation kinetics was run 10^5 times at seawater ionic strength and salinity. The combination of these two models allows for an estimation of pO_2 based on the Fe isotope composition of the IFs compiled here (Wang et al., 2022).

The results show a statistically significant difference between the Griquatown and Timeball Hill GIFs, of which the latter exhibits δ^{56}Fe values close to those expected for Fe(II) inputs, which we consider as clear evidence for complete Fe(II) oxidation (Fig. 6A). We find that the Fe isotope signatures observed in the Timeball Hill ironstone are extremely difficult to explain unless the dissolved O_2 concentration of their contemporaneous shallow seawater was above 5 μmol/kg, corresponding to atmospheric pO_2 above ∼ 1–2 % PAL. Conversely, partial Fe(II) oxidation responsible for the deposition of the Griquatown GIF most likely requires dissolved O_2 and atmospheric pO_2 below 1 μmol/kg and ∼ 0.1–0.5 % PAL, respectively (Fig. 6B). Given that our model assumes that Fe(II) oxidation

takes place via the abiotic reaction with ambient O_2, and that the rates of Fe(II) oxidation by microaerophilic chemoautotrophs are higher than abiotic oxidation rates at low dissolved O_2 levels (e.g., Chan et al., 2016), our estimate of < 1 μmol/kg O_2 is likely to be conservatively high.

It is also noted that in contrast with likely widespread oxic shallow waters in early Paleoproterozoic, those Archean oases described above are spatially limited and characterized by shallow weakly oxygenated waters set against a backdrop of prevailing anoxic conditions in both the water column and atmosphere. While Archean oases may have been transient in nature, leading to the generation of 'whiffs' of O_2 (Anbar et al., 2007), modelling has also suggested that they may have been more static and laterally extensive, correlated to areas of high nutrient input or upwelling coastal waters (Olson et al., 2013). Given the potential role of O_2 (although minor in Archean) in oxidizing Fe(II) in the photic zones, we also invert the Fe isotope data of those BIFs deposited in Archean and early Paleoproterozoic oases to conservatively estimate the maximum dissolved O_2 concentration of the photic zone (Fig. 6). To this end, the inverted isotopic data in Fig. 6A for BIFs older than 2.31 Ga, indicating a f_{ox} (i.e., Fe(II) oxidation extent) range of about 0.7 to 0.95, which would correspond to dissolved O_2 levels of < 1 μmol/kg in the photic zone of these oxygen oases (Fig. 6B).

Our results strongly support an anoxic world before ∼ 2.4 Ga with local O_2 oases containing < 1 μmol/kg O_2, less than or at the very low end of previous modeling results for O_2 concentrations within Archean oases (1–10 μmol/kg O_2; Olson et al., 2013; Reinhard et al., 2013). Nonetheless, given that a dissolved O_2 concentration of 1 μmol/kg is equivalent to a roughly 5000-fold oversaturation with respect to an atmospheric pO_2 of ∼ 10^{-6} PAL (Catling and Zahnle, 2020) (Fig. 6B), it is reasonable to infer that there was severe ocean–atmosphere disequilibrium with respect to O_2 on Archean Earth's surface in biologically productive regions of the ocean. Assuming oxygenic photosynthesis emerged in the Archean, these estimated low O_2 concentrations suggest that net primary productivity—and by extension marine nutrient levels—were significantly lower than that of equivalent modern environments. Based on previous Earth system model simulations, the predominantly anoxic surface ocean implies that the oceanic P inventory of the Archean may have been as low as 25 % of the
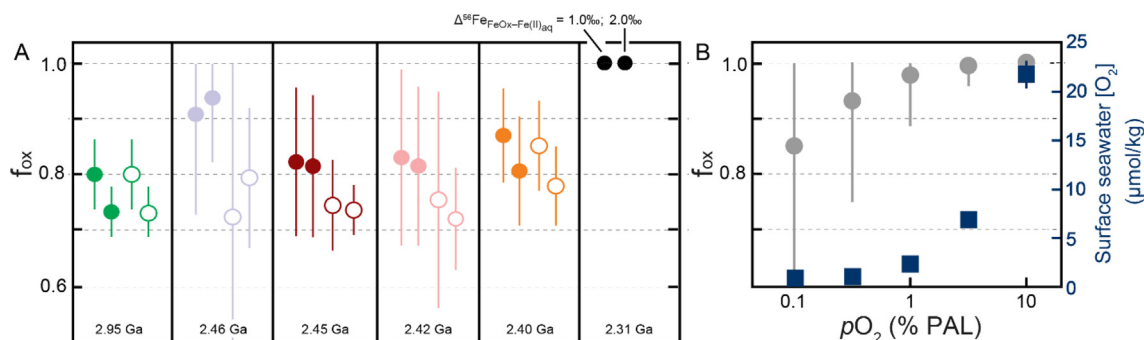

Fig. 6. A model for Fe(II) oxidation in the ∼ 2.95 Ga Sinqeni BIF, ∼2.5–2.4 Ga BIFs in Hamersley and Transvaal basins, ∼2.45 Ga Griquatown and ∼ 2.31 Ga Timeball Hill GIFs as a function of dissolved O_2 abundance of the surface ocean or photic zone. Because of the limited data of the ∼ 3.24 Moodies BIF, it is precluded from this figure. Shown in (A) are estimates of the fraction of Fe(II) oxidized in shallow marine environments (f_{ox}) based on a Rayleigh distillation model assuming two overall isotope effects (α = 1.0 (left) and 2.0 ‰ (right)) for the combined processes of Fe(II) oxidation and precipitation as Fe(III)-(oxyhydr)oxides. Mean results are shown for the combined data (filled circles) and data filtered to exclude non-fractionated samples (open circles). Error bars show ± 1σ for the entire subsampled dataset. Shown in (B) are results from a kinetic model of Fe(II) oxidation, resampled 10,000 times at each atmospheric pO_2 value (relative to PAL) across a range of seawater pH and temperature values. Note that every pO_2 value (grey circle) corresponds to one shallow seawater dissolved O_2 concentration (μmol/kg) (blue circle) assuming gas–water exchange equilibrium. Error bars show ± 1σ. Also note that partial Fe(II) oxidation during the Archean is indicative of low net primary productivity. The systematics of the observed ∼ 2.45 Ga samples are difficult to explain unless dissolved O_2 and atmospheric pO_2 were below 1 μmol/kg and ∼ 0.1 % PAL, respectively, while the ∼ 2.31 Ga Timeball Hill data imply dissolved O_2 at least 5 μmol/kg and a minimum atmospheric pO_2 of ∼ 1 % PAL during GOE.
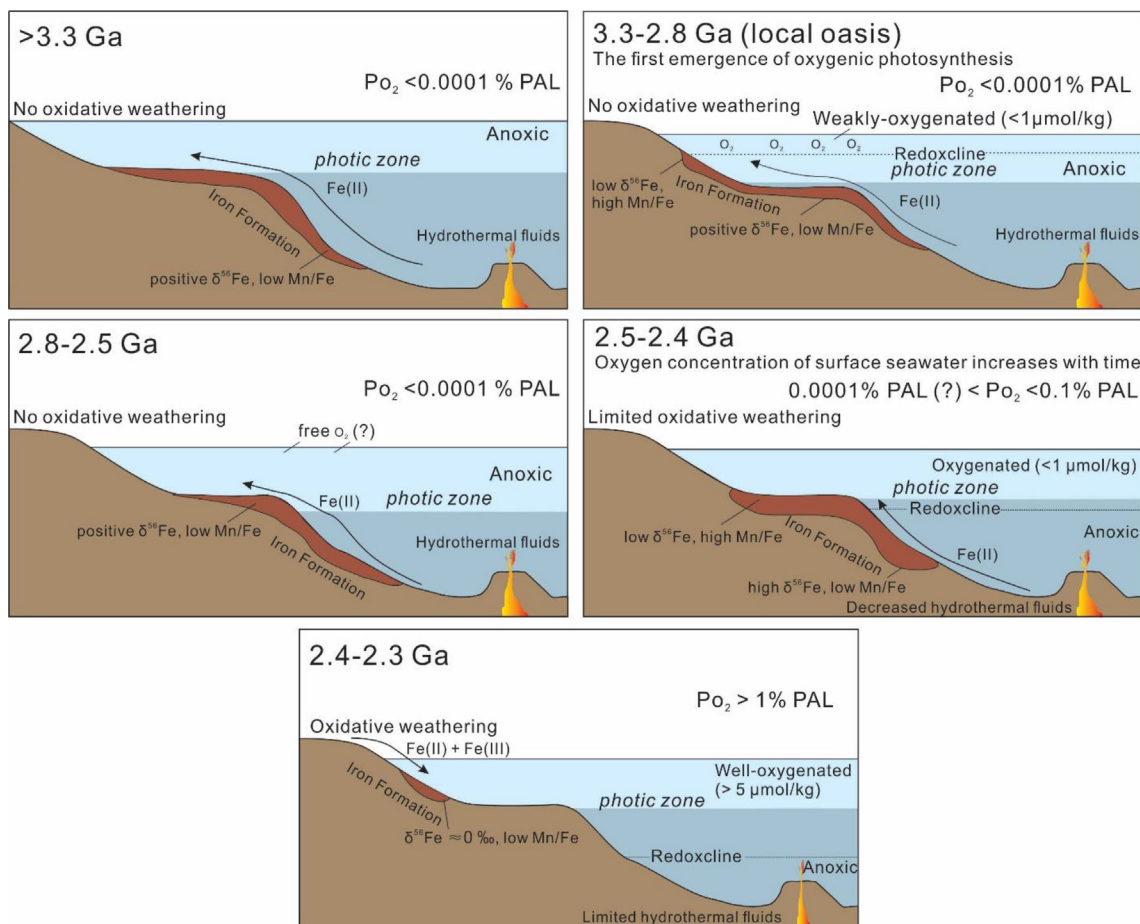
Fig. 7. Schematic diagram showing the temporal progression of oxygenation of the Archean to early Paleoproterozoic ocean and atmosphere. Note that the redoxcline changes with dissolved O$_2$ concentrations in the surface seawater and that the hydrothermal flux decreases over time.

modern (Olson et al., 2013), whereas P levels similar to, or higher than, the modern may have resulted in the establishment of a well-oxygenated surface ocean at ∼ 2.31 Ga.

6. Conclusions

In sum, our findings provide new and complementary insights into how the redox structure of the ocean varied through the Archean to early Paleoproterozoic (Fig. 7). Coupled Fe isotope and Mn/Fe ratio data in IFs extend the first production and local accumulation of O$_2$ in the ocean to at least the latest Paleoarchean. When viewed in light of MIF-S signals (Busigny et al., 2017), these results further confirm that oxygenic photosynthesis was active well before the first permanent oxygenation of the atmosphere during the GOE and that free O$_2$ produced via oxygenic photosynthesis had started to play a role in regulating the oxidation of marine Fe(II) since ∼ 3.3 Ga. However, the IF records suggest that despite their early presence, cyanobacteria probably had a limited effect on early marine Fe cycling, and that photoferrotrophy remained the dominant mechanism for Fe(II) oxidation in the Archean ocean, as oxygenated shallow seawater oases in the Archean were transient and spatially restricted.

Importantly, our results argue for a pervasive oxygenation of the shallow ocean during the GOE, with dissolved O$_2$ concentrations in the surface ocean increasing from below 1 to at least 5 µmol/kg. This clearly marks the revolutionary and progressive transition of the dominant oxidative mechanism of marine Fe(II) from photoferrotrophy to free O$_2$ produced via cyanobacteria at

this time. Such a transition could have been closely linked to the growing degree of net primary productivity in the marine environments, ultimately contributing to the progressive, and permanent, oxidation of Earth's surface oceans and atmosphere.

Declaration of Competing Interest

The authors declare that they have no known competing financial interests or personal relationships that could have appeared to influence the work reported in this paper.

Guilbaud, Andy Heard, and an anonymous reviewer, as well as editorial handling by Brian Kendall.

Appendix A. Supplementary material

Research data is provided within the Supplementary Material. Supplementary material to this article can be found online at https://doi.org/10.1016/j.gca.2022.12.002.

References

Afroz, M., 2019. Sedimentology and geochemistry of the 2.93 Ga Basinal Facies of the Red Lake carbonate platform. (Master Thesis) Lakehead University, Canada, pp. 1–167.

Ahn, J.H., Buseck, P.R., 1990. Hematite nanospheres of possible colloidal origin from a Precambrian banded iron formation. Science 250, 111–113.

Aller, R.C., Heilbrun, C., Panzeca, C., Zhu, Z., Baltzer, F., 2004. Coupling between sedimentary dynamics, early diagenetic processes, and biogeochemical cycling in the Amazon-Guianas mobile mud belt: coastal French Guiana. Mar. Geol. 208 (2–4), 331–360.

Anbar, A.D., Duan, Y., Lyons, T.W., Arnold, G.L., Kendall, B., Creaser, R.A., Kaufman, A.J., Gordon, G.W., Scott, C., Garvin, J., 2007. A whiff of oxygen before the Great Oxidation Event? Science 317, 1903–1906.

Appel, P.W., Fedo, C.M., Moorbath, S., Myers, J.S., 1998. Early Archaean Isua supracrustal belt, west Greenland: pilot study of the Isua multidisciplinary research project. Geol. Greenl. Surv. Bull. 180, 94–99.

Archer, C., Vance, D., 2006. Coupled Fe and S isotope evidence for Archean microbial Fe (III) and sulfate reduction. Geology 34 (3), 153–156.

Asael, D., Tissot, F.L., Reinhard, C.T., Rouxel, O., Dauphas, N., Lyons, T.W., Ponzevera, E., Liorzou, C., Chéron, S., 2013. Coupled molybdenum, iron and uranium stable isotopes as oceanic paleoredox proxies during the Paleoproterozoic Shunga Event. Chem. Geol. 362, 193–210.

Ayres, D., 1972. Genesis of iron-bearing minerals in banded iron formation mesobands in the Dales Gorge Member, Hamersley Group, Western Australia. Econ. Geol. 67, 1214–1233.

Balci, N., Bullen, T.D., Witte-Lien, K., Shanks, W.C., Motelica, M., Mandernack, K.W., 2006. Iron isotope fractionation during microbially stimulated Fe (II) oxidation and Fe (III) precipitation. Geochim. Cosmochim. Acta 70 (3), 622–639.

Bau, M., 1993. Effects of syn-and post-depositional processes on the rare-earth element distribution in Precambrian iron-formations. Eur. J. Mineral. 5 (2), 257–267.

Bau, M., Dulski, P., 1996. Distribution of yttrium and rare-earth elements in the Penge and Kuruman iron-formations, Transvaal Supergroup. South Africa. Precambrian Research 79 (1–2), 37–55.

Bau, M., Romer, R.L., Lüders, V., Beukes, N.J., 1999. Pb, O, and C isotopes in silicified Mooidraai dolomite (Transvaal Supergroup, South Africa): implications for the composition of Paleoproterozoic seawater and 'dating'the increase of oxygen in the Precambrian atmosphere. Earth Planet. Sci. Lett. 174, 43–57.

Beard, B.L., Johnson, C.M., Cox, L., Sun, H., Nealson, K.H., Aguilar, C., 1999. Iron isotope biosignatures. Science 285 (5435), 1889–1892.

Beard, B.L., Johnson, C.M., Von Damm, K.L., Poulson, R.L., 2003. Iron isotope constraints on Fe cycling and mass balance in oxygenated Earth oceans. Geology 31, 629–632.

Beard, B.L., Handler, R.M., Scherer, M.M., Wu, L., Czaja, A.D., Heimann, A., Johnson, C.M., 2010. Iron isotope fractionation between aqueous ferrous iron and goethite. Earth Planet. Sci. Lett. 295 (1–2), 241–250.

Bekker, A., Holland, H., 2012. Oxygen overshoot and recovery during the early Paleoproterozoic. Earth Planet. Sci. Lett. 317, 295–304.

Bekker, A., Holland, H., Wang, P.L., Rumble, D., Stein, H., Hannah, J., Coetzee, L., Beukes, N., 2004. Dating the rise of atmospheric oxygen. Nature 427, 117–120.

Bekker, A., Slack, J.F., Planavsky, N., Krapez, B., Hofmann, A., Konhauser, K.O., Rouxel, O.J., 2010. Iron Formation: The Sedimentary Product of a Complex Interplay among Mantle, Tectonic, Oceanic, and Biospheric Processes. Econ. Geol. 105, 467–508.

Bekker, A., Kaufman, A.J., Karhu, J.A., Beukes, N.J., Swart, Q.D., Coetzee, L.L., Eriksson, K.A., 2001. Chemostratigraphy of the Paleoproterozoic Duitschland Formation, South Africa: implications for coupled climate change and carbon cycling. Am. J. Sci. 301, 261–285.

Bekker, A., Planavsky, N., Rasmussen, B., Krapez, B., Hofmann, A., Slack, J., Rouxel, O., Konhauser, K., 2014. Iron formations: Their origins and implications for ancient seawater chemistry. Treatise on geochem., 12. Elsevier, pp. 561–628.

Beukes, N.J., 1986. The Transvaal sequence in Griqualand west. Mineral deposits of southern Africa, 819–828.

Beukes, N.J., Gutzmer, J., 2008. Origin and paleoenvironmental significance of major iron formations at the Archean-Paleoproterozoic boundary. Rev. Econ. Geol. 15, 5–47.

Boden, J.S., Konhauser, K.O., Robbins, L.J., Sánchez-Baracaldo, P., 2021. Timing the evolution of antioxidant enzymes in cyanobacteria. Nat. Commun. 12 (1), 1–12.

Bolhar, R., Hofmann, A., Siahi, M., Feng, Y.X., Delvigne, C., 2015. A trace element and Pb isotopic investigation into the provenance and deposition of stromatolitic carbonates, ironstones and associated shales of the~ 3.0 Ga Pongola Supergroup. Kaapvaal Craton. Geochimica et Cosmochimica Acta 158, 57–78.

Bonnand, P., Lalonde, S.V., Boyet, M., Heubeck, C., Homann, M., Nonnotte, P., Foster, I., Konhauser, K.O., Köhler, I., 2020. Post-depositional REE mobility in a Paleoarchean banded iron formation revealed by La-Ce geochronology: A cautionary tale for signals of ancient oxygenation. Earth Planet. Sci. Lett. 547, 116452.

Bontognali, T.R., Fischer, W.W., Föllmi, K.B., 2013. Siliciclastic associated banded iron formation from the 3.2 Ga Moodies group, Barberton greenstone belt. South Africa. Precambrian Research 226, 116–124.

Busigny, V., Planavsky, N.J., Jézéquel, D., Crowe, S., Louvat, P., Moureau, J., Viollier, E., Lyons, T.W., 2014. Iron isotopes in an Archean ocean analogue. Geochim. Cosmochim. Acta 133, 443–462.

Busigny, V., Marin-Carbonne, J., Muller, E., Cartigny, P., Rollion-Bard, C., Assayag, N., Philippot, P., 2017. Iron and sulfur isotope constraints on redox conditions associated with the 3.2 Ga barite deposits of the Mapepe Formation (Barberton Greenstone Belt, South Africa). Geochim. Cosmochim. Acta 210, 247–266.

Cairns-Smith, A.G., 1978. Precambrian solution photochemistry, inverse segregation, and banded iron formations. Nature 276 (5690), 807–808.

Caquineau, T., Paquette, J.L., Philippot, P., 2018. U-Pb detrital zircon geochronology of the Turee Creek Group, Hamersley Basin, Western Australia: timing and correlation of the Paleoproterozoic glaciations. Precambr. Res. 307, 34–50.

Catling, D.C., Zahnle, K.J., 2020. The archean atmosphere. Science. Advances 6 (9), eaax1420.

Chan, C.S., Emerson, D., Luther III, G.W., 2016. The role of microaerophilic Fe-oxidizing micro-organisms in producing banded iron formations. Geobiology 14 (5), 509–528.

Cloud, P., 1973. Paleoecological significance of the banded iron-formation. Econ. Geol. 68, 1135–1143.

Coetzee, L.L., 2001. Genetic stratigraphy of the Paleoproterozoic Pretoria Group in the western Transvaal. (Master thesis) Rand Afrikaans University, Johannesburg, South Africa, pp. 1-212.

Corfu, F., Wallace, H., 1986. U-Pb zircon ages for magmatism in the Red Lake greenstone belt, northwestern Ontario. Can. J. Earth Sci. 23, 27–42.

Croal, L.R., Johnson, C.M., Beard, B.L., Newman, D.K., 2004. Iron isotope fractionation by Fe (II)-oxidizing photoautotrophic bacteria. Geochim. Cosmochim. Acta 68, 1227–1242.

Crosby, H.A., Johnson, C.M., Roden, E.E., Beard, B.L., 2005. Coupled Fe (II)– Fe (III) electron and atom exchange as a mechanism for Fe isotope fractionation during dissimilatory iron oxide reduction. Environ. Sci. Tech. 39 (17), 6698–6704.

Crosby, H.A., Roden, E.E., Johnson, C.M., Beard, B.L., 2007. The mechanisms of iron isotope fractionation produced during dissimilatory Fe (III) reduction by Shewanella putrefaciens and Geobacter sulfurreducens. Geobiology 5 (2), 169–189.

Cui, M., Zhang, L., Wu, H., Xu, Y., Li, W., 2014. Timing and tectonic setting of the Sijiaying banded iron deposit in the eastern Hebei province, North China Craton: Constraints from geochemistry and SIMS zircon U-Pb dating. J. Asian Earth Sci. 94, 240–251.

Czaja, A.D., Johnson, C.M., Roden, E.E., Beard, B.L., Voegelin, A.R., Nägler, T.F., Beukes, N.J., Wille, M., 2012. Evidence for free oxygen in the Neoarchean ocean based on coupled iron–molybdenum isotope fractionation. Geochim. Cosmochim. Acta 86, 118–137.

Czaja, A.D., Johnson, C.M., Beard, B.L., Roden, E.E., Li, W., Moorbath, S., 2013. Biological Fe oxidation controlled deposition of banded iron formation in the ca. 3770 Ma Isua Supracrustal Belt (West Greenland). Earth Planet. Sci. Lett. 363, 192–203.

Czaja, A.D., Van Kranendonk, M.J., Beard, B.L., Johnson, C.M., 2018. A multistage origin for Neoarchean layered hematite-magnetite iron formation from the Weld Range, Yilgarn Craton, Western Australia. Chem. Geol. 488, 125–137.

Dauphas, N., John, S.G., Rouxel, O., 2017. Iron isotope systematics. Rev. Mineral. Geochem. 82 (1), 415–510.

Dauphas, N., Rouxel, O., 2006. Mass spectrometry and natural variations of iron isotopes. Mass Spectrom. Rev. 25, 515–550.

Dauphas, N., Van Zuilen, M., Wadhwa, M., Davis, A.M., Marty, B., Janney, P.E., 2004. Clues from Fe isotope variations on the origin of early Archean BIFs from Greenland. Science 306 (5704), 2077–2080.

Dauphas, N., Cates, N.L., Mojzsis, S.J., Busigny, V., 2007. Identification of chemical sedimentary protoliths using iron isotopes in the> 3750 Ma Nuvvuagittuq supracrustal belt. Canada. Earth and Planetary Science Letters 254 (3–4), 358–376.

Daye, M., Klepac-Ceraj, V., Pajusalu, M., Rowland, S., Farrell-Sherman, A., Beukes, N., Tamura, N., Fournier, G., Bosak, T., 2019. Light-driven anaerobic microbial oxidation of manganese. Nature 576, 311–314.

Dideriksen, K., Baker, J., Stipp, S., 2006. Iron isotopes in natural carbonate minerals determined by MC-ICP-MS with a ^{58}Fe-^{54}Fe double spike. Geochim. Cosmochim. Acta 70, 118–132.

Doelsch, E., Stone, W.E., Petit, S., Masion, A., Rose, J., Bottero, J.Y., Nahon, D., 2001. Speciation and crystal chemistry of Fe (III) chloride hydrolyzed in the presence of SiO4 ligands. 2. Characterization of Si– Fe aggregates by FTIR and 29Si Solid-State NMR. Langmuir 17, 1399–1405.

Doelsch, E., Rose, J., Masion, A., Bottero, J.Y., Nahon, D., Bertsch, P.M., 2002. Hydrolysis of iron (II) chloride under anoxic conditions and influence of SiO4 ligands. Langmuir 18, 4292–4299.

Doelsch, E., Masion, A., Rose, J., Stone, W.E., Bottero, J.Y., Bertsch, P.M., 2003. Chemistry and structure of colloids obtained by hydrolysis of Fe (III) in the presence of SiO4 ligands. Colloids Surf A Physicochem Eng Asp 217, 121–128.

Dorland, H.C., 1999. Paleoproterozoic laterites, red beds and ironstones of the Pretoria Group with reference to the history of atmospheric oxygen. University of Johannesburg, South Africa, pp. 1–136. PhD thesis.

Eriksson, P., Catuneanu, O., 2004. Third-order sequence stratigraphy in the Palaeoproterozoic Daspoort formation (Pretoria Group, Transvaal supergroup), Kaapvaal craton. The Precambrian Earth: tempos and events, 724–735.

Farquhar, J., Zerkle, A.L., Bekker, A., 2011. Geological constraints on the origin of oxygenic photosynthesis. Photosynth. Res. 107, 11–36.

Field, E.K., Kato, S., Findlay, A.J., MacDonald, D.J., Chiu, B.K., Luther III, G.W., Chan, C. S., 2016. Planktonic marine iron oxidizers drive iron mineralization under low-oxygen conditions. Geobiology 14 (5), 499–508.

Fischer, W.W., Knoll, A.H., 2009. An iron shuttle for deepwater silica in Late Archean and early Paleoproterozoic iron formation. Geol. Soc. Am. Bull. 121 (1–2), 222–235.

Fischer, W.W., Hemp, J., Johnson, J.E., 2016. Evolution of oxygenic photosynthesis. Annu. Rev. Earth Planet. Sci. 44, 647–683.

Frost, C.D., von Blanckenburg, F., Schoenberg, R., Frost, B.R., Swapp, S.M., 2007. Preservation of Fe isotope heterogeneities during diagenesis and metamorphism of banded iron formation. Contrib. Miner. Petrol. 153 (2), 211–235.

Garrels, R., Perry, E., Mackenzie, F., 1973. Genesis of Precambrian iron-formations and the development of atmospheric oxygen. Econ. Geol. 68, 1173–1179.

Gibson, T.M., Kunzmann, M., Poirier, A., Schumann, D., Tosca, N.J., Halverson, G.P., 2020. Geochemical signatures of transgressive shale intervals from the 811 Ma Fifteenmile Group in Yukon, Canada: Disentangling sedimentary redox cycling from weathering alteration. Geochim. Cosmochim. Acta 280, 161–184.

Gross, G.A., 1983. Tectonic systems and the deposition of iron-formation. Developments in Precambrian Geology. Elsevier, 63–79.

Guilbaud, R., Butler, I.B., Ellam, R.M., 2011. Abiotic pyrite formation produces a large Fe isotope fractionation. Science 332 (6037), 1548–1551.

Gumsley, A.P., Chamberlain, K.R., Bleeker, W., Söderlund, U., de Kock, M.O., Larsson, E.R., Bekker, A., 2017. Timing and tempo of the Great Oxidation Event. Proc. Natl. Acad. Sci. 114, 1811–1816.

Guo, Q., Strauss, H., Kaufman, A.J., Schröder, S., Gutzmer, J., Wing, B., Baker, M.A., Bekker, A., Jin, Q., Kim, S.T., 2009. Reconstructing Earth's surface oxidation across the Archean-Proterozoic transition. Geology 37, 399–402.

Gutzmer, J., Beukes, N.J., 1996. Mineral paragenesis of the Kalahari managanese field, South Africa. Ore Geol. Rev. 11, 405–428.

Halevy, I., Alesker, M., Schuster, E.M., Popovitz-Biro, R., Feldman, Y., 2017. A key role for green rust in the Precambrian oceans and the genesis of iron formations. Nat. Geosci. 10 (2), 135–139.

Halevy, I., Bachan, A., 2017. The geologic history of seawater pH. Science 355 (6329), 1069–1071.

Han, X., Tomaszewski, E., Sorwat, J., Pan, Y., Kappler, A., Byrne, J., 2020. Oxidation of green rust by anoxygenic phototrophic Fe (II)-oxidising bacteria. Geochemical Perspectives Letters 12, 52–57.

Hannah, J.L., Bekker, A., Stein, H.J., Markey, R.J., Holland, H.D., 2004. Primitive Os and 2316 Ma age for marine shale: implications for Paleoproterozoic glacial events and the rise of atmospheric oxygen. Earth Planet. Sci. Lett. 225, 43–52.

Haugaard, R., Pecoits, E., Lalonde, S., Rouxel, O., Konhauser, K., 2016. The Joffre banded iron formation, Hamersley Group, Western Australia: Assessing the palaeoenvironment through detailed petrology and chemostratigraphy. Precambr. Res. 273, 12–37.

Heard, A.W., Dauphas, N., Guilbaud, R., Rouxel, O.J., Butler, I.B., Nie, N.X., Bekker, A., 2020. Triple iron isotope constraints on the role of ocean iron sinks in early atmospheric oxygenation. Science 370, 446–449.

Heard, A.W., Dauphas, N., 2020. Constraints on the coevolution of oxic and sulfidic ocean iron sinks from Archean-Paleoproterozoic iron isotope records. Geology 48 (4), 358–362.

Heubeck, C., 2019. The moodies group—A high-resolution archive of Archaean surface processes and basin-forming mechanisms, The Archaean Geology of the Kaapvaal Craton, Southern Africa. Springer, pp. 133-169.

Heubeck, C., Lowe, D.R., 1999. Sedimentary petrography and provenance of the Archean Moodies Group, Barberton greenstone belt. Special paper-Geological Society of America, 259–286.

Hofmann, A., 2005. The geochemistry of sedimentary rocks from the Fig Tree Group, Barberton greenstone belt: Implications for tectonic, hydrothermal and surface processes during mid-Archaean times. Precambr. Res. 143, 23–49.

Holland, H.D., 2006. The oxygenation of the atmosphere and oceans. Philos. Trans. R. Soc., B 361, 903–915.

Holland, H.D., 1984. The chemical evolution of the atmosphere and oceans. Princeton, New Jersey, Princeton University Press, 582 p.

Homann, M., Sansjofre, P., Van Zuilen, M., Heubeck, C., Gong, J., Killingsworth, B., Foster, I.S., Airo, A., Van Kranendonk, M.J., Ader, M., 2018. Microbial life and biogeochemical cycling on land 3,220 million years ago. Nat. Geosci. 11, 665–671.

Hongve, D., 1997. Cycling of iron, manganese, and phosphate in a meromictic lake. Limnol. Oceanogr. 42, 635–647.

Hyslop, E.V., Valley, J.W., Johnson, C.M., Beard, B.L., 2008. The effects of metamorphism on O and Fe isotope compositions in the Biwabik Iron Formation, northern Minnesota. Contrib. Miner. Petrol. 155 (3), 313–328.

Icopini, G.A., Anbar, A.D., Ruebush, S.S., Tien, M., Brantley, S.L., 2004. Iron isotope fractionation during microbial reduction of iron: The importance of adsorption. Geology 32 (3), 205–208.

Izon, G., Luo, G., Uveges, B.T., Beukes, N., Kitajima, K., Ono, S., Valley, J.W., Ma, X., Summons, R.E., 2022. Bulk and grain-scale minor sulfur isotope data reveal

complexities in the dynamics of Earth's oxygenation. Proceedings of the National Academy of Sciences, 119(13), e2025606119.

Jabłońska, J., Tawfik, D.S., 2021. The evolution of oxygen-utilizing enzymes suggests early biosphere oxygenation. Nat. Ecol. Evol., 1–7

Johnson, C., Beard, B., Weyer, S., 2020. The Ancient Earth, Iron Geochemistry: An Isotopic Perspective. Springer, pp. 215-360.

Johnson, C.M., Zheng, X.Y., Djokic, T., Van Kranendonk, M.J., Czaja, A.D., Roden, E.E., Beard, B.L., 2022. Reply to Comment by Birger Rasmussen and Janet R. Muhling on "Early Archean biogeochemical iron cycling and nutrient availability: New insights from a 3.5 Ga land-sea transition" by Johnson et al. Earth-Science Reviews, 231, 104087.

Jones, C., Nomosatryo, S., Crowe, S.A., Bjerrum, C.J., Canfield, D.E., 2015. Iron oxides, divalent cations, silica, and the early earth phosphorus crisis. Geology 43, 135–138.

Jung, H., Xu, X., Wan, B., Wang, Q., Borkiewicz, O.J., Li, Y., Chen, H.L., Liu, A.H., Tang, Y., 2021. Photocatalytic oxidation of dissolved Mn (II) on natural iron oxide minerals. Geochim. Cosmochim. Acta 312, 343–356.

Kappler, A., Pasquero, C., Konhauser, K.O., Newman, D.K., 2005. Deposition of banded iron formations by anoxygenic phototrophic Fe (II)-oxidizing bacteria. Geology 33, 865–868.

Klein, C., Beukes, N.J., 1989. Geochemistry and sedimentology of a facies transition from limestone to iron-formation deposition in the early Proterozoic Transvaal Supergroup, South Africa. Econ. Geol. 84, 1733–1774.

Koehler, M.C., Buick, R., Kipp, M.A., Stüeken, E.E., Zaloumis, J., 2018. Transient surface ocean oxygenation recorded in the∼ 2.66-Ga Jeerinah Formation, Australia. Proc. Natl. Acad. Sci. 115, 7711–7716.

Konhauser, K.O., Amskold, L., Lalonde, S.V., Posth, N.R., Kappler, A., Anbar, A., 2007. Decoupling photochemical Fe (II) oxidation from shallow-water BIF deposition. Earth Planet. Sci. Lett. 258 (1–2), 87–100.

Konhauser, K.O., Robbins, L.J., Alessi, D.S., Flynn, S.L., Gingras, M.K., Martinez, R.E., Kappler, A., Swanner, E.D., Li, Y.-L., Crowe, S.A., 2018. Phytoplankton contributions to the trace-element composition of Precambrian banded iron formations. Bulletin 130, 941-951.

Konhauser, K.O., Hamade, T., Raiswell, R., Morris, R.C., Ferris, F.G., Southam, G., Canfield, D.E., 2002. Could bacteria have formed the Precambrian banded iron formations? Geology 30, 1079–1082.

Konhauser, K.O., Lalonde, S.V., Planavsky, N.J., Pecoits, E., Lyons, T.W., Mojzsis, S.J., Rouxel, O.J., Barley, M.E., Rosìere, C., Fralick, P.W., 2011. Aerobic bacterial pyrite oxidation and acid rock drainage during the Great Oxidation Event. Nature 478, 369–373.

Konhauser, K., Planavsky, N., Hardisty, D., Robbins, L., Warchola, T., Haugaard, R., Lalonde, S., Partin, C., Oonk, P., Tsikos, H., 2017. Iron formations: A global record of Neoarchean to Palaeoproterozoic environmental history. Earth Sci. Rev. 172, 140–177.

Kunzmann, M., Gibson, T.M., Halverson, G.P., Hodgskiss, M.S., Bui, T.H., Carozza, D. A., Sperling, E.A., Poirier, A., Cox, G.M., Wing, B.A., 2017. Iron isotope biogeochemistry of Neoproterozoic marine shales. Geochim. Cosmochim. Acta 209, 85–105.

Kurzweil, F., Wille, M., Gantert, N., Beukes, N.J., Schoenberg, R., 2016. Manganese oxide shuttling in pre-GOE oceans–evidence from molybdenum and iron isotopes. Earth Planet. Sci. Lett. 452, 69–78.

Lantink, M.L., Oonk, P.B., Floor, G.H., Tsikos, H., Mason, P.R., 2018. Fe isotopes of a 2.4 Ga hematite-rich IF constrain marine redox conditions around the GOE. Precambr. Res. 305, 218–235.

Li, W., Czaja, A.D., Van Kranendonk, M.J., Beard, B.L., Roden, E.E., Johnson, C.M., 2013. An anoxic, Fe (II)-rich, U-poor ocean 3.46 billion years ago. Geochim. Cosmochim. Acta 120, 65–79.

Li, Y.L., Konhauser, K.O., Zhai, M., 2017. The formation of magnetite in the early Archean oceans. Earth Planet. Sci. Lett. 466, 103–114.

Li, W., Beard, B.L., Johnson, C.M., 2015. Biologically recycled continental iron is a major component in banded iron formations. Proceedings of the National Academy of Sciences 112(27), 8193-8198.

Liu, W., Hao, J., Elzinga, E.J., Piotrowiak, P., Nanda, V., Yee, N., Falkowski, P.G., 2020. Anoxic photogeochemical oxidation of manganese carbonate yields manganese oxide. Proceedings of the National Academy of Sciences 117, 22698-22704.

Lowe, D.R., 2013. Crustal fracturing and chert dike formation triggered by large meteorite impacts, ca. 3.260 Ga, Barberton greenstone belt. South Africa. Bulletin 125, 894–912.

Lowe, D.R., Byerly, G.R., 1999. Stratigraphy of the west-central part of the Barberton Greenstone Belt, South Africa. Geol. Soc. Am. Spec. Paper 329, 1–36.

Luo, G., Ono, S., Beukes, N.J., Wang, D.T., Xie, S., Summons, R.E., 2016. Rapid oxygenation of Earth's atmosphere 2.33 billion years ago. Science. Advances 2, e1600134.

Lyons, T.W., Reinhard, C.T., Planavsky, N.J., 2014. The rise of oxygen in Earth's early ocean and atmosphere. Nature 506, 307–315.

Lyons, T.W., Diamond, C.W., Konhauser, K.O., 2020. Shedding light on manganese cycling in the early oceans. Proc. Natl. Acad. Sci. 117 (42), 25960–25962.

Maliva, R.G., Knoll, A.H., Simonson, B.M., 2005. Secular change in the Precambrian silica cycle: insights from chert petrology. Geol. Soc. Am. Bull. 117, 835–845.

Marin-Carbonne, J., Busigny, V., Miot, J., Rollion-Bard, C., Muller, E., Drabon, N., Jacob, D., Pont, S., Robyr, M., Bontognali, T.R.R., François, C., Reynaud, S., Zuilen, M.V., Philippot, P., 2020. In Situ Fe and S isotope analyses in pyrite from the 3.2 Ga Mendon Formation (Barberton Greenstone Belt, South Africa): Evidence for early microbial iron reduction. Geobiology 18 (3), 306–325.

Maynard, J.B., 2010. The chemistry of manganese ores through time: a signal of increasing diversity of earth-surface environments. Econ. Geol. 105, 535–552.

McIntyre, T., Fralick, P., 2017. Sedimentology and Geochemistry of the 2930 Ma Red Lake-Wallace Lake Carbonate Platform, Western Superior Province, Canada. The Depositional Record 3, 258–287.

McLennan, S.M., 1989. Rare earth elements in sedimentary rocks: influence of provenance and sedimentary processes. Geochemistry and Mineralogy of Rare Earth Elements, Reviews in Mineralogy 21, 169–200.

Millet, M.A., Baker, J.A., Payne, C.E., 2012. Ultra-precise stable Fe isotope measurements by high resolution multiple-collector inductively coupled plasma mass spectrometry with a ^{57}Fe–^{58}Fe double spike. Chem. Geol. 304, 18–25.

Morris, R., Horwitz, R., 1983. The origin of the iron-formation-rich Hamersley Group of Western Australia—deposition on a platform. Precambr. Res. 21, 273–297.

Muhling, J.R., Rasmussen, B., 2020. Widespread Deposition of Greenalite to Form Banded Iron Formations before the Great Oxidation Event. Precambr. Res. 105619.

Myers, J.S., 2001. Protoliths of the 3.8–3.7 Ga Isua greenstone belt, west Greenland. Precambr. Res. 105, 129–141.

Nabhan, S., Köhler, I., Heubeck, C., 2017. Local and regional controls on the maturation state of carbonaceous matter in the Barberton Greenstone Belt. In: Annual Meeting DGGV Bremen 2017, abstract volume, p 449.

Nel, B.P., 2013. Petrography and geochemistry of iron formations of the Paleoproterozoic Koegas Subgroup, Transvaal Supergroup, Griqualand West, South Africa. University of Johannesburg, South Africa, pp. 1–132. PhD Thesis.

Nelson, D., Trendall, A., Altermann, W., 1999. Chronological correlations between the Pilbara and Kaapvaal cratons. Precambr. Res. 97, 165–189.

Nutman, A.P., Allaart, J.H., Bridgwater, D., Dimroth, E., Rosing, M., 1984. Stratigraphic and geochemical evidence for the depositional environment of the early Archaean Isua supracrustal belt, southern West Greenland. Precambr. Res. 25, 365–396.

Nutman, A.P., Mojzsis, S.J., Friend, C.R., 1997. Recognition of ≥ 3850 Ma water-lain sediments in West Greenland and their significance for the early Archaean Earth. Geochim. Cosmochim. Acta 61, 2475–2484.

Nutman, A.P., Friend, C.R., Bennett, V.C., 2002. Evidence for 3650–3600 Ma assembly of the northern end of the Itsaq Gneiss Complex, Greenland: implication for early Archaean tectonics. Tectonics 21, 5-1-5-28.

Nutman, A.P., Bennett, V.C., Friend, C.R., 2017. Seeing through the magnetite: Reassessing Eoarchean atmosphere composition from Isua (Greenland) ≥ 3.7 Ga banded iron formations. Geosci. Front. 8, 1233–1240.

Olson, S.L., Kump, L.R., Kasting, J.F., 2013. Quantifying the areal extent and dissolved oxygen concentrations of Archean oxygen oases. Chem. Geol. 362, 35–43.

Ossa, F.O., Hofmann, A., Spangenberg, J.E., Poulton, S.W., Stüeken, E.E., Schoenberg, R., Eickmann, B., Wille, M., Butler, M., Bekker, A., 2019. Limited oxygen production in the Mesoarchean ocean. Proceedings of the National Academy of Sciences 116, 6647-6652.

Pecoits, E., Gingras, M., Barley, M., Kappler, A., Posth, N., Konhauser, K., 2009. Petrography and geochemistry of the Dales Gorge banded iron formation: Paragenetic sequence, source and implications for palaeo-ocean chemistry. Precambr. Res. 172, 163–187.

Peng, Z., Wang, C., Tong, X., Zhang, L., Zhang, B., 2018. Element geochemistry and neodymium isotope systematics of the Neoarchean banded iron formations in the Qingyuan greenstone belt, North China Craton. Ore Geol. Rev. 102, 562–584.

Peng, Z., Wang, C., Zhang, L., Zhu, M., Tong, X., 2019. Geochemistry of metamorphosed volcanic rocks in the Neoarchean Qingyuan greenstone belt, North China Craton: Implications for geodynamic evolution and VMS mineralization. Precambr. Res. 326, 196–221.

Percak-Dennett, E., Beard, B., Xu, H., Konishi, H., Johnson, C., Roden, E., 2011. Iron isotope fractionation during microbial dissimilatory iron oxide reduction in simulated Archaean seawater. Geobiology 9, 205–220.

Philippot, P., Ávila, J.N., Killingsworth, B.A., Tessalina, S., Baton, F., Caquineau, T., Muller, E., Pecoits, E., Cartigny, P., Lalonde, S.V., 2018. Globally asynchronous sulphur isotope signals require re-definition of the Great Oxidation Event. Nat. Commun. 9, 1–10.

Pickard, A., 2002. SHRIMP U-Pb zircon ages of tuffaceous mudrocks in the Brockman Iron Formation of the Hamersley Range, Western Australia. Aust. J. Earth Sci. 49, 491–507.

Pickard, A., 2003. SHRIMP U-Pb zircon ages for the Palaeoproterozoic Kuruman Iron Formation, northern Cape Province, South Africa: evidence for simultaneous BIF deposition on Kaapvaal and Pilbara cratons. Precambr. Res. 125, 275–315.

Planavsky, N.J., Asael, D., Hofmann, A., Reinhard, C.T., Lalonde, S.V., Knudsen, A., Wang, X., Ossa, F.O., Pecoits, E., Smith, A.J., 2014. Evidence for oxygenic photosynthesis half a billion years before the Great Oxidation Event. Nat. Geosci. 7, 283–286.

Planavsky, N., Bekker, A., Rouxel, O.J., Kamber, B., Hofmann, A., Knudsen, A., Lyons, T.W., 2010. Rare earth element and yttrium compositions of Archean and Paleoproterozoic Fe formations revisited: new perspectives on the significance and mechanisms of deposition. Geochim. Cosmochim. Acta 74 (22), 6387–6405.

Planavsky, N., Rouxel, O.J., Bekker, A., Hofmann, A., Little, C.T., Lyons, T.W., 2012. Iron isotope composition of some Archean and Proterozoic iron formations. Geochim. Cosmochim. Acta 80, 158–169.

Polat, A., Frei, R., 2005. The origin of early Archean banded iron formations and of continental crust, Isua, southern West Greenland. Precambr. Res. 138, 151–175.

Polteau, S., Moore, J.M., Tsikos, H., 2006. The geology and geochemistry of the Palaeoproterozoic Makganyene diamictite. Precambr. Res. 148, 257–274.

Poulton, S.W., Bekker, A., Cumming, V.M., Zerkle, A.L., Canfield, D.E., Johnston, D.T., 2021. A 200-million-year delay in permanent atmospheric oxygenation. Nature 592 (7853), 232–236.

Rasmussen, B., Bekker, A., Fletcher, I.R., 2013a. Correlation of Paleoproterozoic glaciations based on U-Pb zircon ages for tuff beds in the Transvaal and Huronian Supergroups. Earth Planet. Sci. Lett. 382, 173–180.

Rasmussen, B., Krapež, B., Meier, D.B., 2014. Replacement origin for hematite in 2.5 Ga banded iron formation: Evidence for postdepositional oxidation of iron-bearing minerals. Bulletin 126, 438-446.

Rasmussen, B., Meier, D.B., Krapež, B., Muhling, J.R., 2013b. Iron silicate microgranules as precursor sediments to 2.5-billion-year-old banded iron formations. Geology 41, 435–438.

Rasmussen, B., Muhling, J.R., Suvorova, A., Krapež, B., 2017. Greenalite precipitation linked to the deposition of banded iron formations downslope from a late Archean carbonate platform. Precambr. Res. 290, 49–62.

Rasmussen, B., Muhling, J.R., Tosca, N.J., Tsikos, H., 2019. Evidence for anoxic shallow oceans at 2.45 Ga: Implications for the rise of oxygenic photosynthesis. Geology 47, 622–626.

Reddy, T.R., Zheng, X.Y., Roden, E.E., Beard, B.L., Johnson, C.M., 2016. Silicon isotope fractionation during microbial reduction of Fe (III)–Si gels under Archean seawater conditions and implications for iron formation genesis. Geochim. Cosmochim. Acta 190, 85–99.

Reinhard, C.T., Planavsky, N.J., Olson, S.L., Lyons, T.W., Erwin, D.H., 2016. Earth's oxygen cycle and the evolution of animal life. Proceedings of the National Academy of Sciences 113(32), 8933-8938.

Reinhard, C.T., Lalonde, S.V., Lyons, T.W., 2013. Oxidative sulfide dissolution on the early Earth. Chem. Geol. 362, 44–55.

Robbins, L.J., Lalonde, S.V., Planavsky, N.J., Partin, C.A., Reinhard, C.T., Kendall, B., Scott, C., Hardisty, D.S., Gill, B.C., Alessi, D.S., 2016. Trace elements at the intersection of marine biological and geochemical evolution. Earth Sci. Rev. 163, 323–348.

Robbins, L.J., Funk, S.P., Flynn, S.L., Warchola, T.J., Li, Z., Lalonde, S.V., Rostron, B.J., Smith, A.J., Beukes, N.J., de Kock, M.O., 2019. Hydrogeological constraints on the formation of Palaeoproterozoic banded iron formations. Nat. Geosci. 12, 558–563.

Rolison, J.M., Stirling, C.H., Middag, R., Gault-Ringold, M., George, E., Rijkenberg, M.J., 2018. Iron isotope fractionation during pyrite formation in a sulfidic Precambrian ocean analogue. Earth Planet. Sci. Lett. 488, 1–13.

Rollinson, H., 2003. Metamorphic history suggested by garnet-growth chronologies in the Isua Greenstone Belt, West Greenland. Precambr. Res. 126, 181–196.

Rouxel, O.J., Bekker, A., Edwards, K.J., 2005. Iron isotope constraints on the Archean and Paleoproterozoic ocean redox state. Science 307, 1088–1091.

Sanborn-Barrie, M., Skulski, T., Parker, J., 2001. Three hundred million years of tectonic history recorded by the Red Lake greenstone belt. Ontario: Geological Survey of Canada. Current Research 2001, 1–14.

Sánchez-Baracaldo, P., Cardona, T., 2020. On the origin of oxygenic photosynthesis and Cyanobacteria. New Phytol. 225 (4), 1440–1446.

Satkoski, A.M., Beukes, N.J., Li, W., Beard, B.L., Johnson, C.M., 2015. A redox-stratified ocean 3.2 billion years ago. Earth Planet. Sci. Lett. 430, 43–53.

Schad, M., Halama, M., Bishop, B., Konhauser, K.O., Kappler, A., 2019. Temperature fluctuations in the Archean ocean as trigger for varve-like deposition of iron and silica minerals in banded iron formations. Geochim. Cosmochim. Acta 265, 386–412.

Schad, M., Byrne, J.M., ThomasArrigo, L.K., Kretzschmar, R., Konhauser, K.O., Kappler, A., 2022. Microbial Fe cycling in a simulated Precambrian ocean environment: Implications for secondary mineral (trans)formation and deposition during BIF genesis. Geochim. Cosmochim. Acta 331, 165–191.

Schröder, S., Bedorf, D., Beukes, N.J., Gutzmer, J., 2011. From BIF to red beds: Sedimentology and sequence stratigraphy of the Paleoproterozoic Koegas Subgroup (South Africa). Sediment. Geol. 236 (1–2), 25–44.

Schröder, S., Beukes, N.J., Armstrong, R.A., 2016. Detrital zircon constraints on the tectonostratigraphy of the Paleoproterozoic Pretoria Group, South Africa. Precambr. Res. 278, 362–393.

Severmann, S., Johnson, C., Beard, B., German, C., Edmonds, H., Chiba, H., Green, D., 2004. The effect of plume processes on the Fe isotope composition of hydrothermally derived Fe in the deep ocean as inferred from the Rainbow vent site, Mid-Atlantic Ridge, 36 14′ N. Earth Planet. Sci. Lett. 225, 63–76.

Severmann, S., Lyons, T.W., Anbar, A., McManus, J., Gordon, G., 2008. Modern iron isotope perspective on the benthic iron shuttle and the redox evolution of ancient oceans. Geology 36, 487–490.

Siahi, M., Tsikos, H., Rafuza, S., Oonk, P.B., Mhlanga, X.R., van Niekerk, D., Mason, P. R., Harris, C., 2020. Insights into the processes and controls on the absolute abundance and distribution of manganese in Precambrian iron formations. Precambr. Res. 350, 105878.

Slotznick, S.P., Johnson, J.E., Rasmussen, B., Raub, T.D., Webb, S.M., Zi, J.W., Kirschvink, J.L., Fischer, W.W., 2022. Reexamination of 2.5-Ga "whiff" of oxygen interval points to anoxic ocean before GOE. Sci. Adv. 8 (1), eabj7190.

Smith, A., Beukes, N., Gutzmer, J., Czaja, A., Johnson, C., Nhleko, N., 2017. Oncoidal granular iron formation in the Mesoarchaean Pongola Supergroup, southern Africa: Textural and geochemical evidence for biological activity during iron deposition. Geobiology 15, 731–749.

Smith, A.J.B., Beukes, N.J., Gutzmer, J., Johnson, C.M., Czaja, A.D., Nhleko, N., de Beer, F., Hoffman, J.W., Awramik, S.M., 2020. Life on a Mesoarchean marine shelf – insights from the world's oldest known granular iron formation. Scitific Report 10, 10519.

Smith, R.E., Perdrix, J., Parks, T., 1982. Burial metamorphism in the Hamersley basin, Western Australia. J. Petrol. 23, 75–102.

Steinhoefel, G., Horn, I., von Blanckenburg, F., 2009. Micro-scale tracing of Fe and Si isotope signatures in banded iron formation using femtosecond laser ablation. Geochim. Cosmochim. Acta 73 (18), 5343–5360.

Sumner, D.Y., Bowring, S.A., 1996. U-Pb geochronologic constraints on deposition of the Campbellrand Subgroup, Transvaal Supergroup, South Africa. Precambr. Res. 79, 25–35.

Sun, S., Konhauser, K.O., Kappler, A., Li, Y.L., 2015. Primary hematite in Neoarchean to Paleoproterozoic oceans. Bulletin 127, 850-861.

Sun, J., Zhu, X., Li, Z., 2018. Confirmation and global significance of a large-scale early Neoproterozoic banded iron formation on Hainan Island, China. Precambr. Res. 307, 82–92.

Swanner, E.D., Mloszewska, A.M., Cirpka, O.A., Schoenberg, R., Konhauser, K.O., Kappler, A., 2015. Modulation of oxygen production in Archaean oceans by episodes of Fe (II) toxicity. Nat. Geosci. 8, 126–130.

Swanner, E.D., Bayer, T., Wu, W., Hao, L., Obst, M., Sundman, A., Byrne, J.M., Michel, F.M., Kleinhanns, I.C., Kappler, A., Schoenberg, R., 2017. Iron isotope fractionation during Fe (II) oxidation mediated by the oxygen-producing marine cyanobacterium Synechococcus PCC 7002. Environ. Sci. Tech. 51 (9), 4897–4906.

Tabata, H., Sekine, Y., Kanzaki, Y., Sugita, S., 2021. An experimental study of photo-oxidation of Fe (II): Implications for the formation of Fe (III)(hydro) oxides on early Mars and Earth. Geochim. Cosmochim. Acta 299, 35–51.

Tebo, B.M., Johnson, H.A., McCarthy, J.K., Templeton, A.S., 2005. Geomicrobiology of manganese (II) oxidation. Trends Microbiol. 13, 421–428.

Thibon, F., Blichert-Toft, J., Tsikos, H., Foden, J., Albalat, E., Albarede, F., 2019. Dynamics of oceanic iron prior to the Great Oxygenation Event. Earth Planet. Sci. Lett. 506, 360–370.

Tosca, N.J., Guggenheim, S., Pufahl, P.K., 2016. An authigenic origin for Precambrian greenalite: Implications for iron formation and the chemistry of ancient seawater. Bulletin 128 (3–4), 511–530.

Trendall, A., 1973. Precambrian iron-formations of Australia. Econ. Geol. 68, 1023–1034.

Trendall, A., Blockley, J., 1970. The iron formations of the Precambrian Hamersley Group, Western Australia, with special reference to the associated crocidolite. Geological Survey of Western Australia. Bulletin, 119, 365 p.

Trendall, A., Compston, W., Nelson, D., De Laeter, J., Bennett, V., 2004. SHRIMP zircon ages constraining the depositional chronology of the Hamersley Group, Western Australia. Aust. J. Earth Sci. 51, 621–644.

Tsikos, H., Beukes, N.J., Moore, J.M., Harris, C., 2003. Deposition, diagenesis, and secondary enrichment of metals in the Paleoproterozoic Hotazel iron formation, Kalahari Manganese Field, South Africa. Econ. Geol. 98, 1449–1462.

Tsikos, H., Matthews, A., Erel, Y., Moore, J.M., 2010. Iron isotopes constrain biogeochemical redox cycling of iron and manganese in a Palaeoproterozoic stratified basin. Earth Planet. Sci. Lett. 298 (1–2), 125–134.

Veizer, J., 1978. Secular variations in the composition of sedimentary carbonate rocks, II. Fe, Mn, Ca, Mg, Si and minor constituents. Precambrian Research 6(3-4), 381-413.

Wang, C., Lechte, M.A., Reinhard, C.T., Asael, D., Cole, D.B., Halverson, G.P., Porter, S.M., Galili, N., Halevy, I., Rainbird, R.H., Lyons, T.W., Planavsky, N.J., 2022. Strong evidence for a weakly oxygenated ocean–atmosphere system during the Proterozoic. Proceedings of the National Academy of Sciences of the United States of America 119(6), e2116101119.

Wang, C., Wu, H., Li, W., Peng, Z., Zhang, L., Zhai, M., 2017. Changes of Ge/Si, REE+ Y and Sm-Nd isotopes in alternating Fe-and Si-rich mesobands reveal source heterogeneity of the~ 2.54 Ga Sijiaying banded iron formation in Eastern Hebei, China. Ore Geology Reviews 80, 363–376.

Warchola, T., Lalonde, S.V., Pecoits, E., von Gunten, K., Robbins, L.J., Alessi, D.S., Philippot, P., Konhauser, K.O., 2018. Petrology and geochemistry of the Boolgeeda Iron Formation, Hamersley Basin, Western Australia. Precambr. Res. 316, 155–173.

Warke, M.R., Di Rocco, T., Zerkle, A.L., Lepland, A., Prave, A.R., Martin, A.P., Ueno, Y., Condon, D.J., Claire, M.W., 2020. The Great Oxidation Event preceded a Paleoproterozoic "snowball Earth". Proceedings of the National Academy of Sciences 117, 13314-13320.

Warke, M.R., Schröder, S., 2018. Synsedimentary fault control on the deposition of the Duitschland Formation (South Africa): Implications for depositional settings, Paleoproterozoic stratigraphic correlations, and the GOE. Precambr. Res. 310, 348–364.

Wiesli, R.A., Beard, B.L., Johnson, C.M., 2004. Experimental determination of Fe isotope fractionation between aqueous Fe (II), siderite and "green rust" in abiotic systems. Chem. Geol. 211 (3–4), 343–362.

Wittkop, C., Swanner, E.D., Grengs, A., Lambrecht, N., Fakhraee, M., Myrbo, A., Bray, A.W., Poulton, S.W., Katsev, S., 2020. Evaluating a primary carbonate pathway for manganese enrichments in reducing environments. Earth Planet. Sci. Lett. 538, 116201.

Wu, L., Beard, B.L., Roden, E.E., Johnson, C.M., 2011. Stable iron isotope fractionation between aqueous Fe(II) and hydrous ferric oxide. Environ. Sci. Tech. 45, 1847–1852.

Wu, L., Percak-Dennett, E.M., Beard, B.L., Roden, E.E., Johnson, C.M., 2012. Stable iron isotope fractionation between aqueous Fe(II) and model Archean ocean Fe–Si coprecipitates and implications for iron isotope variations in the ancient rock record. Geochim. Cosmochim. Acta 84, 14–28.

Zegeye, A., Bonneville, S., Benning, L.G., Sturm, A., Fowle, D.A., Jones, C., Canfield, D.E., Ruby, C., MacLean, L.C., Nomosatryo, S., Crowe, S., Poulton, S.W., 2012. Green rust formation controls nutrient availability in a ferruginous water column. Geology 40, 599–602.

Zheng, X.Y., Beard, B.L., Reddy, T.R., Roden, E.E., Johnson, C.M., 2016. Abiologic silicon isotope fractionation between aqueous Si and Fe (III)–Si gel in simulated Archean seawater: Implications for Si isotope records in Precambrian sedimentary rocks. Geochim. Cosmochim. Acta 187, 102–122.